Computers and Fluids 267 (2023) 106069

Contents lists available at ScienceDirect

Computers and Fluids

journal homepage: www.elsevier.com/locate/compfluid

Finite-rate and equilibrium study of graphite ablation under arc-jet conditions

Aleksander L. Zibitsker [a,*,1], Joel A. McQuaid [b,2], Eric C. Stern [d,3], Grant E. Palmer [c,4], Benjamin J. Libben [d,5], Christoph Brehm [b,6], Alexandre Martin [a,7]

[a] University of Kentucky, Lexington, KY 40506, United States of America
[b] University of Maryland, College Park, MD 20742, United States of America
[c] AMA, Inc. at NASA Ames Research Center, Moffett Field, CA 94035, United States of America
[d] NASA Ames Research Center, Moffett Field, CA 94035, United States of America

ARTICLE INFO

Keywords:
Arc-jet flow
Graphite ablation
Overset grid solver
Material response
Coupled simulation

ABSTRACT

Arc-jet facilities play a primary role in recreating aerothermal conditions experienced by atmospheric entry vehicles and are widely used to test the performance of thermal protection materials. In this work, we utilize a developed coupled framework between an overset flow solver CHAMPS NBS-Cart, and a material solver KATS-MR to study the ablation of graphite under arc-jet conditions. We implement a 12-species gas phase model to accurately represent the air-carbon mixture, including argon species present in the flow. The gas phase is modeled with a two-temperature thermo-chemical non-equilibrium model without considering electronic and ionization effects. The gas-surface interactions are modeled with a newly developed air-carbon ablation model accounting for oxidation, nitridation, and recombination reactions. In addition, the model is augmented with carbon sublimation reactions experienced at high heating conditions. The chemical state at the surface is tightly coupled with the flow solver, resulting in the improved accuracy and effectiveness of the simulation. The coupled approach is applied to study two experimental test cases conducted at the IHF arc-jet facility at NASA Ames. The predicted results are validated against measured recession, surface, and in-depth temperatures and compared to the prediction of the uncoupled, equilibrium-based approach. Finally, the accuracy of the prediction is explored with respect to the environmental properties, such as the diffusion coefficient, and material thermal conductivity.

1. Introduction

Arc-jet facilities are capable of recreating extreme heating conditions experienced by atmospheric entry vehicles and are widely used to test the performance of thermal protection system (TPS) materials. The enthalpy of the arc-jet is set to achieve the flight-relevant heating rate on the arc-jet model (typically an iso-q, hemispherical, or flat-face calorimeter). The total enthalpy of the arc-jet flow is set by heating the injected gas to extreme temperatures in the plenum section with a high-voltage DC electric arc discharge. Additional energy to the flow is added by accelerating the gas through the converging-diverging nozzle connected to the plenum. The test gas is set based on the given atmospheric composition with some addition of argon to protect the electrodes of the arc heater. The NASA Ames Research Center houses one of the largest arc-jet heating facilities in the world, which includes the Aerodynamic Heating Facility (AHF), the Interaction Heating Facility (IHF), and the Panel Test Facility (PTF) [1].

The injected gas flow rates, the total enthalpy of the flow, and the pressure in the plenum are used to estimate the inflow conditions in the numerical simulation of the arc-jet flow. While the mass flow rates and total pressure are measured quantities in the plenum, the

* Corresponding author.
E-mail addresses: alex.zibitsker@uky.edu (A.L. Zibitsker), jamcq@umd.edu (J.A. McQuaid), eric.c.stern@nasa.gov (E.C. Stern), grant.e.palmer@nasa.gov (G.E. Palmer), benjamin.j.libben@nasa.gov (B.J. Libben), cbrehm1@umd.edu (C. Brehm), alexandre.martin@uky.edu (A. Martin).
[1] Graduate Research Assistant, Mechanical and Aerospace Engineering, 151 Ralph G. Anderson Building.
[2] Graduate Research Assistant, Aerospace Engineering, 3179 Glenn L. Martin Hall, Building.
[3] Research Engineer, MS 234-1, Thermal Protection System Materials Branch.
[4] Research Scientist, MS 230-2, Aerothermodynamics Branch.
[5] Aerospace Engineer, Entry Systems and Vehicle Development Branch.
[6] Associate Professor, Aerospace Engineering, 3179 Glenn L. Martin Hall, Building.
[7] Professor, Mechanical Engineering, 151 Ralph G. Anderson Building.

https://doi.org/10.1016/j.compfluid.2023.106069
Received 30 June 2023; Received in revised form 6 September 2023; Accepted 1 October 2023
Available online 6 October 2023

total enthalpy is usually an estimated quantity based on the heat balance method, calibration against measured heat flux, and other techniques [2]. The gas flow rates set the elemental composition of the flow, which, along with the estimated total enthalpy and measured pressure allow extraction of the temperature, the equilibrium species composition, and velocity at the entrance to the nozzle [3]. Equilibrium conditions typically exist until reaching the nozzle throat, where the flow starts to experience thermal non-equilibrium. The dissociated gas species in the flow, however, are still in the frozen chemical state until they reach the nozzle exit [4]. The flow in a thermal non-equilibrium is typically modeled with the Park two-temperature model [5,6] that was implemented in the number of thermochemical non-equilibrium (TCNE) flow solvers [7–10].

Simulating the behavior of the TPS material in the presence of a chemically reactive flow is not a trivial task not only due to the complex physical and chemical processes in the flow and at the material surface but also due to the various uncertainties in the estimated flow conditions and models. One of the early and still widely used approaches to simulate material thermal response and ablation was developed using the film coefficient theory [11–13]. In this approach, the heating to the material surface is modeled using the enthalpy difference between the boundary layer edge and the wall, multiplied by the effective heat- and mass-transfer coefficients, accounting for the conduction and diffusion heat fluxes. The ablation rate of the material is computed assuming equilibrium chemistry conditions at the surface and mass-transfer coefficient. The main advantages of the film-coefficient approach appear in the relative accuracy of the method near the stagnation region of the geometry and an uncoupled nature of the method that allows running material simulations quickly for the preliminary design of the heatshield. In addition, the approach is relatively insensitive to the assumed wall temperature, such as a cold wall condition or radiative equilibrium, meaning that the cold wall or radiative equilibrium heat transfer coefficient will not differ much. Capabilities for material response simulations with surface ablation and internal decomposition for charring ablators were developed in a series of one-dimensional codes [14–16] and more recently in multi-dimensional codes [17–22].

The performance of the film-coefficient approach starts to deteriorate away from the stagnation region due to the formation of non-equilibrium conditions along the surface and a poor prediction of the change of heat- and mass-transfer coefficients due to the blowing of ablation gases [23,24]. Shape change of the geometry introduces additional challenges to the approach due to the dependence of the boundary conditions profiles on the surface topology [25,26]. At these conditions, coupling between the flow and material solvers provides an undeniable advantage as it is capable of accurate prediction of the changing boundary conditions at the evolving material surface and accounting for the non-equilibrium chemistry effects in the boundary layer.

Coupling between the flow and material solvers is an active area of research due to the multiple factors involved in the interaction between the flow and material domains. The high-speed nature of the flow during the atmospheric entry or at the exit from the arc-jet nozzle leads to a vast difference in the time scales between the flow and material physics. In addition, finite-rate chemical processes occurring at the surface strongly affect the local conditions in the flow, thus affecting the accuracy of the estimation of the heating environment. One of the simplest approaches explored by Chen et al. [27] used a loosely coupled procedure and equilibrium thermo-chemistry, where the boundary conditions between the solvers were exchanged only after a certain amount of surface recession had occurred. After each transfer of the new surface geometry, the flow mesh was adjusted, and a new flow solution was obtained. The same author implemented a higher fidelity approach to the ablation problem [28], where instead, finite-rate reactions were used to model the surface ablation, but the material thermal response was estimated by a steady state heating assumption.

Validation of the material response simulations is typically performed based on the measured quantities, such as surface and in-depth material temperature and amount of recession. However, little well-characterized data is available in the open literature, making it hard to conduct a thorough verification of the developed simulation. One of the widely studied materials with available experimental data is graphite, which has well-characterized material property data and recent chemistry models to account for surface ablation. The ablation mechanism of graphite also resembles other carbon-based ablators allowing the application of the validated models to a wider range of materials. Coupled studies of graphite ablation were performed with varying levels of fidelity in the past. Graphite ablation under arc-jet conditions was explored with GIANTS-TITAN simulation with equilibrium ablation thermo-chemistry at the surface and included material thermal response and recession, but injection of the ablating species into the boundary layer was not accounted for in the study [29]. The same study was later refined with the inclusion of finite-rate surface chemistry, but the material thermal response was modeled with a steady-state assumption [28]. Several additional coupled studies of graphite with various levels of fidelity were performed in the following studies [30,31].

In this work, we employ a recently developed coupled simulation capability between the overset flow solver CHAMPS NBS-Cart and material response solver KATS-MR [26,32] to simulate the ablation of graphite under arc-jet conditions. The coupled simulation employs a high-fidelity approach, relying on finite-rate chemistry and full coupling of the material thermal response solution to the flow domain. The finite-rate ablation at the surface is modeled with the air-carbon ablation (ACA) model recently developed by Prata et al. [33], augmented with sublimation reactions to account for a range of conditions occurring at the surface. The surface chemistry is tightly coupled with the near-body solver increasing the accuracy of the estimated boundary conditions and allowing larger material steps to be taken. The simulations focus on studying two experimental test cases, aiming to predict surface and in-depth temperatures and the amount of recession. The sensitivity of the solution is examined by considering the diffusivity of the gas species and the available thermal properties of the material. Additionally, the coupled results are compared to equivalent uncoupled solutions based on the equilibrium thermo-chemistry to assess the relative performance and limitations of the latter approach.

2. Flow solver framework

2.1. Governing equations

In this work, the interaction of the chemically reactive flow and graphite surface is modeled with a 12-species model. The model includes 5 air species, such as N_2, O_2, NO, N and O with additional argon species present in one of the test cases. An additional 6 species result from the gas-surface and solid phase reactions, such as CO_2, CO, CN, C, C_2, and C_3. The injection of ablation species leads to additional chemical reactions in the boundary layer and also affects the transport properties of the boundary layer gas. The thermal non-equilibrium, resulting from the high-temperature gas of the arc-jet flow, is modeled using Park's two-temperature model [34] accounting for the translational–rotational temperature, T, and a vibrational temperature, T_v. Electronic, ionization and radiative effects within the fluid phase are neglected in this work to reduce the computational cost of the employed gas model. The chemically-reacting flow in thermo-chemical non-equilibrium is modeled using the compressible Navier–Stokes equations shown below

$$\frac{\partial \boldsymbol{U}}{\partial \boldsymbol{P}} \frac{\partial \boldsymbol{P}}{\partial t} + \boldsymbol{\nabla} \cdot \left(\boldsymbol{F} - \boldsymbol{F}_{\boldsymbol{d}} \right) = \boldsymbol{W}, \tag{1}$$

where $\boldsymbol{U}$ is the conservative state vector, $\boldsymbol{P}$ is the primitive state vector, $\boldsymbol{F}$ is the convective flux, $\boldsymbol{F}_{\boldsymbol{d}}$ is the viscous flux and $\boldsymbol{W}$ is the

thermo-chemical source term. The temporal derivative in the governing equation is represented in a split form to allow a direct solution for the primitive quantities in the problem and increase the speed of the computation. Eq. (2) presents the primitive and conservative state vectors, such that ρ_k is the species density, ρ is the total fluid density, $\boldsymbol{V} = \{u, v, w\}^T$ is the fluid velocity vector with its specified components in the Cartesian reference frame, and E and E_v are the total energy and vibrational energy components per unit volume

$$\boldsymbol{U} = \begin{Bmatrix} \rho_1 \\ \vdots \\ \rho_k \\ \rho u \\ \rho v \\ \rho w \\ E \\ E_v \end{Bmatrix} \text{ and } \boldsymbol{P} = \begin{Bmatrix} \rho_1 \\ \vdots \\ \rho_k \\ u \\ v \\ w \\ T \\ T_v \end{Bmatrix}. \tag{2}$$

The convective, viscous, and source term vectors are given in Eq. (3) where p is the mixture pressure, $\boldsymbol{J_k}$ is the mass diffusion flux vector of species k, $\boldsymbol{\tau}$ is the viscous stress tensor, κ_{tr} and κ_v are the fluid conductivities for the translational/rotational and vibrational energy modes respectively, h_k is the enthalpy of species k, ω_k is the source term for the chemical reactions, S_{t2v} is the source term for the energy exchange between the translational and vibrational energy modes, S_{c2v} is the energy exchange due to chemical reactions, and $\hat{u}$ is defined as the contravariant velocity [35].

$$\boldsymbol{F} = \begin{Bmatrix} \rho_1\hat{u} \\ \vdots \\ \rho_k\hat{u} \\ \rho u\hat{u} + p\delta_{1i} \\ \rho v\hat{u} + p\delta_{2i} \\ \rho w\hat{u} + p\delta_{3i} \\ (E+p)\hat{u} \\ E_v\hat{u} \end{Bmatrix}, \; \boldsymbol{F_d} = \begin{Bmatrix} -\boldsymbol{J_1} \\ \vdots \\ -\boldsymbol{J_k} \\ \boldsymbol{\tau_{1i}} \\ \boldsymbol{\tau_{2i}} \\ \boldsymbol{\tau_{3i}} \\ \kappa_{tr}\nabla T + \kappa_v \nabla T_v - \sum_{k=1}^{ns} \boldsymbol{J_k} h_k + \boldsymbol{\tau}\cdot\boldsymbol{V} \\ \kappa_v \nabla T_v - \sum_{k=1}^{ns} \boldsymbol{J_k} e_{v,k} \end{Bmatrix}, \text{and}$$

$$\boldsymbol{W} = \begin{Bmatrix} \omega_1 \\ \vdots \\ \omega_k \\ 0 \\ 0 \\ 0 \\ 0 \\ S_{t2v} + S_{c2v} \end{Bmatrix}. \tag{3}$$

The species viscosity and conductivity properties are computed using Blottner and Eucken models. The mixture viscosity and conductivity are computed with Wilke's mixing rule. Sutton and Gnoffo (1998) [36] have noted that Fick's law does not guarantee that the mass diffusion fluxes will sum to zero resulting in errors in capturing the correct mass fraction gradients among other errors. Modified Fick's law is used in this work to improve the solution accuracy and is given by

$$\boldsymbol{J_{k\neq e}} = \boldsymbol{I_k} - Y_k \sum_{r\neq e}^{ns} \boldsymbol{I_r}, \tag{4}$$

where ns is the number of species, Y_k is the species mass fraction and e denotes the electron species, not included in this work. The term $\boldsymbol{I_k}$ is the individual species diffusive flux given by

$$\boldsymbol{I_k} = -\rho D_k \nabla Y_k, \tag{5}$$

where D_k is the species diffusion coefficient. In this work, the species diffusion coefficients are approximated with a single mixture coefficient D computed based on a predefined Lewis number as

$$D = \frac{\mathrm{Le}\kappa_{tr}}{\rho c_{p,\mathrm{tr}}}, \tag{6}$$

where $c_{p,\mathrm{tr}}$ is the mixture translational/rotational specific heat at constant pressure.

The chemical source term contains 17 reactions, chosen based on the work of Chen and Milos [28]. The list of the implemented reactions is shown below, where reactions 1–8 model dissociation of each molecular species, while reactions 9–17 are exchange reactions. The Argon species is assumed to not participate in chemical reactions.

1. $N_2 + M \rightleftharpoons N + N + M$
2. $O_2 + M \rightleftharpoons O + O + M$
3. $NO + M \rightleftharpoons N + O + M$
4. $C_3 + M \rightleftharpoons C_2 + C + M$
5. $CO_2 + M \rightleftharpoons CO + O + M$
6. $C_2 + M \rightleftharpoons C + C + M$
7. $CO + M \rightleftharpoons C + O + M$
8. $CN + M \rightleftharpoons C + N + M$
9. $NO + O \rightleftharpoons O_2 + N$
10. $N_2 + O \rightleftharpoons NO + N$
11. $CO + O \rightleftharpoons C + O_2$
12. $CN + O \rightleftharpoons NO + C$
13. $CO_2 + O \rightleftharpoons O_2 + CO$
14. $CO + C \rightleftharpoons C_2 + O$
15. $N_2 + C \rightleftharpoons CN + N$
16. $CN + C \rightleftharpoons C_2 + N$
17. $CO + N \rightleftharpoons CN + O$

The chemical source term, ω_k is defined as

$$\omega_k = M_k \sum_r \dot{w}_{kr}, \tag{7}$$

where the term $\dot{w}_{kr}$ is the production rate of species k in reaction r and is given by

$$\dot{w}_{kr} = (\nu''_{kr} - \nu'_{sr}) \left[k_{fr} \prod_{j=1}^{ns} \left(\frac{\rho_j}{M_j} \right)^{\nu'_{jr}} - k_{br} \prod_{j=1}^{ns} \left(\frac{\rho_j}{M_j} \right)^{\nu''_{jr}} \right], \tag{8}$$

where k_{fr} and k_{br} represent the forward and backward reaction rates and ν' and ν'' are the stoichiometric coefficients for reactants and products, respectively. The Arrhenius curve fit coefficients for dissociation and exchange reactions are given in Tables 6 and 7 in Appendix A. Further details on the chemical-reaction model can be found in the work of McQuaid et al. [32].

2.2. NBS-Cart solver

The flow domain is solved with an overset near-body Cartesian solver developed within the CHAMPS framework, as explained extensively by McQuaid et al. [32] and briefly summarized here. To begin with, the entire domain is discretized using a block-structured Cartesian grid. The near-body grid is automatically generated based on a surface mesh, which can consist of any combination of elements and is provided as an input during the initialization phase. By using the surface nodes, the node point distributions in the wall-normal direction are projected into the freestream, enabling the resolution of the complete boundary layer. The Cartesian solver handles the off-body region, while Adaptive Mesh Refinement (AMR) is employed to track the shock structure and geometry as the surface recedes. The NBS domain is sequentially solved alongside the Cartesian grid solver, ensuring that the surface grid is evenly distributed across all processors to maintain load balancing and scalability. The mesh layout, depicted in Fig. 1, provides a visual representation of how the grid is organized. The Cartesian mesh blocks remain relatively coarse until reaching the geometry surface and each block contains a grid with dimensions of $n_x \times n_y$ points. The NBS grid employs a body-conformal stretched grid approach to accurately capture near-wall gradients. The red dots in the figure indicate the guard cells set by the NBS. Although only one layer of cells is shown, multiple layers are typically used to enable higher-order accurate schemes. At the end of each ray, there is an image point positioned between the guard cell and the last interior cell, which contains interpolated data obtained from the Cartesian grid solution. The red guard cells are then filled in order to enforce the NBS inflow boundary condition. An overset interpolation algorithm is utilized to couple the NBS solution back to the Cartesian near-wall cells, eliminating the need to handle any irregular points near the immersed surface.

The NBS solver employs a conservative finite difference numerical scheme on a generalized curvilinear grid to solve the complete

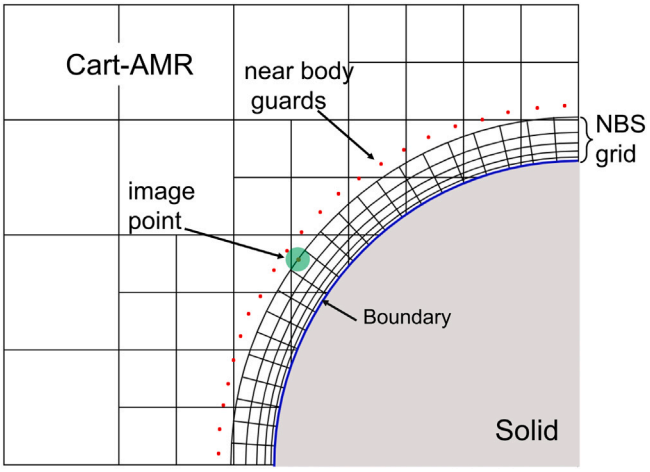

Fig. 1. Cartesian grid with Adaptive Mesh Refinement and near-body curvilinear grid overlaid on top. Note that each block on the Cartesian mesh contains $n_x \times n_y$ grid points.

set of governing equations described previously. For the computation of convective terms, a second-order MUSCL scheme with a modified Steger-Warming flux scheme is employed [37]. Viscous fluxes are computed on the cell faces to ensure a second-order conservative treatment of viscosity. On the other hand, the Cartesian grid solver utilizes a fifth-order WENO scheme of Jiang and Shu [38] to accurately capture the shock structure away from the body, while employing a similar conservative treatment of viscosity as the NBS solver. The lack of alignment of the Cartesian structure with strong shocks can introduce shock artifacts under certain conditions which impacts the accuracy of the heat flux profile on the surface. This issue is corrected by fully reducing to a first-order convective scheme in the presence of strong shocks by using the classical Ducros sensor [39]. The NBS solver adopts a structured grid layout similar to a two-dimensional (2D) grid, which allows for the use of an efficient line-implicit Gauss–Seidel solver suitable for both steady and unsteady flow simulations.

3. Material response solver framework

3.1. Governing equation

In this study, the material thermal response is modeled with a KATS-MR solver. The model includes a solution of transient heat conduction equation equipped with a surface ablation module and mesh motion scheme. The governing equation, represented in the Arbitrary Lagrangian–Eulerian (ALE) framework, is given below

$$\frac{\partial U}{\partial t} - \boldsymbol{\nabla} \cdot \left(\boldsymbol{F_d} + \boldsymbol{F_g} \right) = 0, \tag{9}$$

where $U = \rho_s c_s T$ is the thermal energy storage term, ρ_s is the solid density and c_s is the solid specific heat. The term, $\boldsymbol{F_d} = k_s \boldsymbol{\nabla} T$ is the heat diffusion flux, where k_s is the solid thermal conductivity. The last term $\boldsymbol{F_g} = U\boldsymbol{\omega}$ is the grid advection flux, where $\boldsymbol{\omega}$ is the grid face velocity, defined by $\boldsymbol{\omega} \cdot \hat{n} = \bar{\omega}$ in the integral form of the governing equation. The average grid face velocity $\bar{\omega}$ is computed using the face averaging algorithm proposed by Zhang et al. [40] and is given by

$$\bar{\boldsymbol{\omega}} = \frac{\Delta \bar{V}}{A \Delta t}, \tag{10}$$

where $\Delta \bar{V}$ is the averaged facial volumetric increment, A is the face area and Δt is the incremental time step.

The grid advection flux is responsible for the redistribution of conserved quantities, such as thermal energy, between the cells of the moving mesh. The mesh motion in KATS-MR utilizes the radial basis functions (RBF) approach to interpolate the recession from the surface elements to the nodes in the entire domain. The approach is augmented with implicit enforcement of sliding nodes located at the interface and the axis of the geometry. Further details on the implementation of the mesh motion algorithm can be found in our previous works [41,42].

3.2. Thermal and physical properties

The material simulated in this work is Poco graphite, modeled with isotropic temperature-dependent properties, and constant density. The thermal properties of Poco graphite can be found in several sources [43–47], showing a decent level of variability depending on the grade of the material and measurement technique. In this work, properties from two sources were used to simulate each test case. As reported in the study of Chen et al. [29], which represents the first test case, the material properties were taken from the work of Touloukian et al. [44]. However, it remained unclear what exact properties data was used in the reference study. Instead, the properties were extracted from the work of Minyushkin and Kryukov [48] that reference the same author. The second study uses the properties of Poco graphite from Sheppard et al. [47] that provides more recently evaluated data. Unfortunately, the measured temperature range of thermal conductivity and surface emissivity in Sheppard's data is quite limited and does not cover the expected range. To overcome this issue, curve fits were obtained for conductivity and emissivity, constructed for two grades of Poco graphite later used in the study. The curve fit equations are shown in Eqs. (11) and (12) respectively. The coefficients for the curve fits are given in Tables 8 and 9 in Appendix B. Fig. 2 shows the extracted properties data from both sources including two grades of Poco graphite, ultra-fine and a fine one, as reported by Sheppard et al. [47]. The symbols represent the sampled data from the sources and the dashed curves represent the estimations with the curve fits or simple linear interpolation. It can be seen that the thermal conductivity and emissivity have the most substantial difference between the sources which will be later reflected in the analysis of the results. Finally, the used density of Poco graphite varies between 1660 to 1730 kg/m^3 and will be specified later for each test case.

$$\kappa(T) = \frac{c_0}{c_1 + c_2 T} \tag{11}$$

and

$$\epsilon(T) = c_0 + c_1 T. \tag{12}$$

4. Fluid - material coupling framework

4.1. Surface balance equations

Coupling of the fluid and material domain with finite-rate surface chemistry is performed by solving a set of conservation equations for the exchange of mass, momentum, and energy at the interface. The mass conservation equation for the surface species represents a balance between the mass reaching the surface by diffusion and surface reactions versus the mass flux leaving the surface by the net blowing. In this form, the mass balance equation for pure surface ablator is given by the following equation for each species

$$\underbrace{-\rho_w D_k \frac{\partial Y_k}{\partial \eta}}_{\text{diffusion}} + \underbrace{m_k''}_{\text{production}} = \underbrace{m_w'' Y_{k,w}}_{\text{blowing}}, \tag{13}$$

where m_k'' is the individual species production flux at the wall, m_w'' is the net species blowing flux away from the wall, given in Eq. (14) and η represents the normal direction between the flow cell and the wall. The mass balance is solved for the species mass fraction at the wall $Y_{k,w}$. The mass balance equation can be summed over all species to compute the net blowing flux away from the wall as in the following equation

$$m_w'' = \rho_w u_w = \sum_{k=1}^{ns} m_k''. \tag{14}$$

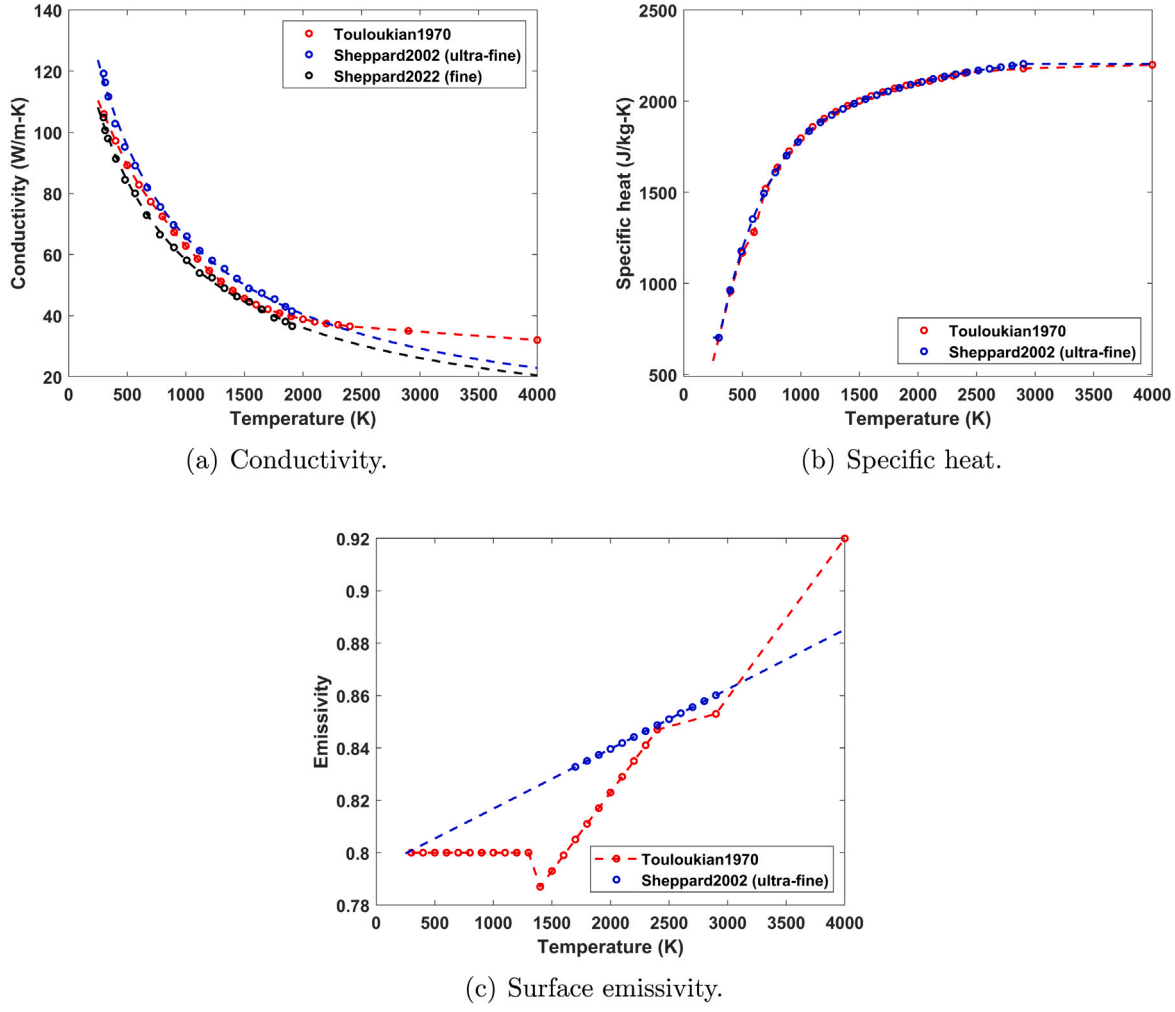

(a) Conductivity. (b) Specific heat.

(c) Surface emissivity.

Fig. 2. Thermal properties of Poco graphite [43–45,47].

The net species blowing flux away from the wall introduces an exchange of momentum at the surface, which can be defined between the near-wall cell and the wall in the following form

$$p_\eta = p_f + \rho_f u_f^2 = p_w + \rho_w u_w^2, \tag{15}$$

where p is the gas static pressure and the subscripts w, f and η represent wall, flow and net conditions respectively. The thermodynamic state of the gas at the wall is represented by the perfect gas law given by

$$p_w = \rho_w R_w T_w, \tag{16}$$

where $R_w = R_u/\bar{M}_w$ is the specific gas constant and $\bar{M}_w$ is the mixture molecular weight at the wall conditions. By combining the momentum balance equation with the equation of state and the total species blowing flux at the wall, the gas blowing velocity, pressure, and density at the wall can be computed using the following set of equations

$$u_w = \frac{2R_w T_w m''_w}{p_\eta + \sqrt{p_\eta^2 - 4R_w T_w m''^2_w}}, \quad p_w = \frac{p_\eta + \sqrt{p_\eta^2 - 4R_w T_w m''^2_w}}{2} \quad \text{and}$$
$$\rho_w = \frac{p_\eta + \sqrt{p_\eta^2 - 4R_w T_w m''^2_w}}{2R_w T_w}. \tag{17}$$

Finally, the energy balance between the TCNE solver and the ablating material surface can be defined in the following form

$$\underbrace{-\kappa_{tr}\nabla T\cdot\hat{\boldsymbol{n}}}_{\substack{\text{translational-rotational}\\ \text{energy conduction}}} - \underbrace{\kappa_v \nabla T_v\cdot\hat{\boldsymbol{n}}}_{\substack{\text{vibrational energy}\\ \text{conduction}}} - \underbrace{\sum_{k=1}^{ns}\rho h_k D_k \nabla Y_k\cdot\hat{\boldsymbol{n}}}_{\text{diffusion heating}} =$$
$$\underbrace{-\kappa_s\nabla T\cdot\hat{\boldsymbol{n}}}_{\substack{\text{solid energy}\\ \text{conduction}}} + \underbrace{\epsilon\sigma(T_w^4 - T_\infty^4)}_{\text{re-radiation}} + \underbrace{m''_w\left(h_w - h_{s,w}\right)}_{\text{ablation flux}}, \tag{18}$$

where the first two terms on the left-hand side define the flow conduction fluxes by the translational–rotational and vibrational energy modes and the third term is the net species diffusion heat flux toward the wall. On the right-hand side, the first term is the solid conduction flux, the second term is the re-radiation flux, and the last term is the material ablation flux consisting of the net species enthalpy blowing flux and solid ablation. In the equation, $\hat{n}$ represents the wall normal vector from the flow to the material domain, ϵ is the surface emissivity, σ is the Stefan–Boltzmann constant, h_w is the mixture gas enthalpy evaluated at the wall conditions, and $h_{s,w}$ is the solid enthalpy at the wall conditions. It should be noted, that radiation from the gas phase toward the surface is neglected here and that the energy equation is solved for the solid conduction flux into the material.

4.2. Surface finite-rate chemistry

Finite-rate chemistry for graphite surface is required to close the set of surface balance equations. In general, graphite material exposed to a hot reactive air environment can undergo a series of gas-surface reactions, such as oxidation and nitridation [49–51], phase change through sublimation at sufficiently high temperatures [52] and surface-induced catalysis [53,54]. The heterogeneous gas-surface reactions are irreversible and lead to the direct loss of material from the surface. Sublimation reactions, in turn, can be reversible, depending on the local pressure of carbon species, and lead to condensation back to the material surface. Finally, surface catalysis does not consume the material, but leads to the recombination of the local atomic species. All aforementioned surface reactions eventually lead to the change of chemical state at the surface and give rise to the mass diffusion fluxes away or toward the wall and the corresponding diffusive heating caused by the enthalpy carried by the diffusing species.

The gas-surface reactions can be modeled by a number of available models such as the one developed by Park [55,56] and Zhluktov and Abe [57]. Park's model has oxidation and nitridation reactions but does not consider catalytic recombination. In addition, the nitridation model has been shown to strongly overpredict the experimental data [58]. Zhlutkov and Abe's model has no nitridation but includes some catalytic recombination reactions. In this study, we use the recently developed air-carbon ablation (ACA) model by Prata et al. [33]. In this model, reaction probabilities were constructed based on continuous beam experiments where atomic oxygen and nitrogen, as well as molecular oxygen species, were directed at the resistively heated vitreous carbon surface at temperatures ranging from 800 to 1873 K. The resultant products, desorbed from the surface, were detected with rotatable mass spectrometers, and the relative fluxes of the resultant species were measured. The constructed model consists of 20 reactions, including oxidation with the formation of carbon monoxide and carbon dioxide, nitridation reactions with the production of the cyanogen radical CN, as well as catalytic recombination reactions to form molecular oxygen and nitrogen at the surface. The list of the 20 reactions implemented in the model is shown below

1. $O + (s) \rightarrow O(s)$
2. $O(s) \rightarrow O + (s)$
3. $O + O(s) + C(b) \rightarrow CO + O + (s)$
4. $O + O(s) + C(b) \rightarrow CO_2 + (s)$
5. $O + (s) \rightarrow O^*(s)$
6. $O^*(s) \rightarrow O + (s)$
7. $O + O^*(s) + C(b) \rightarrow CO + O + (s)$
8. $O^*(s) + O^*(s) \rightarrow O_2 + 2(s)$
9. $O(s) + O(s) \rightarrow O_2 + 2(s)$
10. $N + (s) \rightarrow N(s)$
11. $N(s) \rightarrow N + (s)$
12. $N + N(s) + C(b) \rightarrow CN + N + (s)$
13. $N + N(s) \rightarrow N_2 + (s)$
14. $N(s) + N(s) \rightarrow N_2 + 2(s)$
15. $N(s) + C(b) \rightarrow CN + (s)$
16. $O_2 + 2(s) \rightarrow 2O(s)$
17. $O_2 + O(s) + C(b) \rightarrow CO + O_2 + (s)$
18. $O_2 + O(s) + C(b) \rightarrow CO_2 + O + (s)$
19. $O_2 + 2(s) \rightarrow 2O^*(s)$
20. $O_2 + O^*(s) + C(b) \rightarrow CO + O_2 + (s)$

The rate equations for each species depend on the surface coverage of available sites, where carbon or air species can adsorb to. Details on the solution of the system of equations for the surface site density and the rate equations, as well as the rate constants, can be found in the work of Prata et al. [33]. Verification of the model implementation in 0-D simulation, as well as in the coupled mode at steady-state surface conditions was verified in the work of McQuaid et al. [32]. Finally, note that the ACA model was developed based on experimental data between 800 to 1873 K, and outside of this range the rates are extrapolated. As was observed in this work, the behavior of the rates in the extrapolated region is reasonable, and based on that, the ACA model is used in the full temperature range predicted in the simulations.

Finally, the gas-surface reactions listed above are augmented with solid phase reactions such as sublimation. This type of reactions is modeled using the Knudsen–Langmuir formulation for non-equilibrium surface evaporation [52]. In this work, three sublimation reactions of carbon are considered as shown below

1. $C(b) + (s) \leftrightarrow C + (s)$
2. $2C(b) + 2(s) \leftrightarrow C_2 + 2(s)$
3. $3C(b) + 3(s) \leftrightarrow C_3 + 3(s)$,

where C(b) represents a solid carbon atom and (s) represents an available surface bond site. The rates of sublimation/condensation of carbon species are given by the Knudsen–Langmuir equation as

$$m''_k = \alpha_k \left(p_{v,k} - p_k\right) \sqrt{\frac{M_k}{2\pi R_u T_w}}, \tag{19}$$

where α_k is the experimentally determined vaporization coefficient and $p_{v,k}$ and p_k are the vapor and partial pressures of carbon species k. The vapor pressure of each carbon species is given by

$$p_{v,k} = 101300.0 \exp\left(P_k/T_w + Q_k\right), \tag{20}$$

where the pressure has units of (Pa) and the temperature has units of (K). The values of coefficients α_k, P_k, and Q_k are given in Table 10 in Appendix B. Finally, given the total blowing flux of species away from the surface, the recession rate, normal to the surface, can be obtained with the following simple relation

$$\dot{s} = \frac{m''_w}{\rho_s}. \tag{21}$$

4.3. Coupling algorithm

The coupling between the CHAMPS NBS-Cart and KATS-MR solvers has been developed to handle large-scale problems with recessing surface and non-matching interfaces. The coupling between the solvers is performed through a shared library that handles the data exchange in a global or local manner. Mapping the non-conformal grid solutions between the solvers is performed by utilizing k-d trees to identify n-nearest points to each surface centroid and build an interpolation cloud. From the assembled point cloud, coefficients for the interpolation polynomials are computed and stored. This process is performed on the NBS surface partition because the KATS partition does not guarantee optimal load balancing of the surface points whereas the NBS is solved in a sequential manner to the Cartesian grid solver and so its partition exists equally across all processors.

Since grids on the material and NBS surfaces are generated independently, the coupled solution allows for a mismatch between the face elements. The mismatched surface elements may lead to interpolation errors due to significant surface recession. To treat this issue, the interpolation point is projected onto the line segment connecting the two nearest points within its own interpolation cloud. This modified point coordinate is then used to generate the interpolating polynomial coefficients. More details on the implemented interpolation procedure and the mapping performed between the solvers can be found in the previous work [32].

The time integration scheme between the two solvers with the main solution blocks of each solver is shown in Fig. 3. It should be noted, that in this work the time integration procedure has been changed compared to the previous implementation [26,32,59] and is explained in detail here. Prior to starting the coupled interaction the NBS-Cart solver converges the flow domain to a steady-state with the given initial boundary conditions at the interface. The coupling between the solvers is performed in two stages. In the first stage, the NBS solver calls directly for the surface balance (SB) solver, which is part of the KATS-MR framework, and updates the surface chemical state and blowing based on the solution of the finite-rate chemistry, momentum, and mass balance equations. The mesh is not moved at this stage and the surface temperature is taken from the previous step material solution. The NBS solver performs pseudo-steps, calling every step for

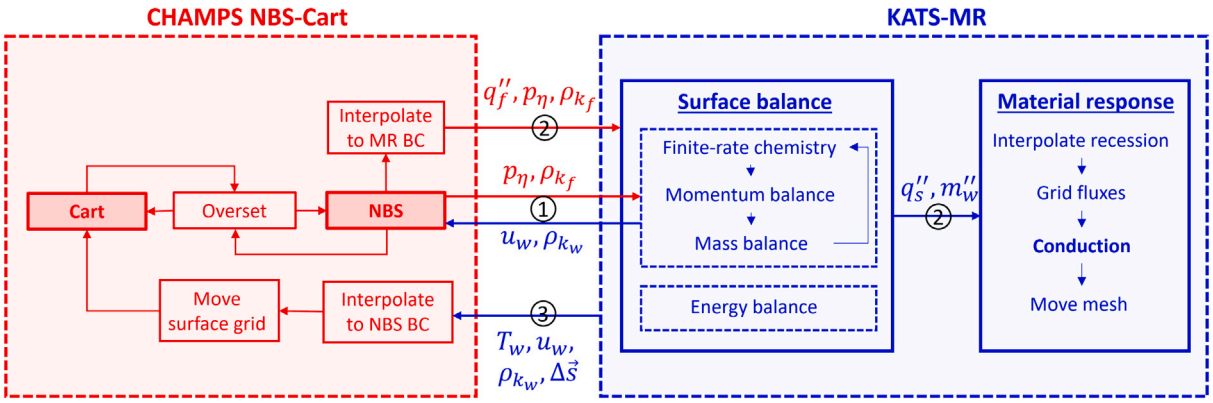

Fig. 3. CHAMPS-KATS coupling scheme.

the surface balance solver to converge onto the new surface state. Following this stage, the NBS solver computes the converged heat flux at the wall, as well as momentum and species densities in the first flow cell, interpolated in front of the material surface elements. KATS-MR performs an additional call to the surface balance equations including the energy balance and updates the ablation rate and conduction heat flux into the material. The evaluated surface recession is interpolated using RBF functions to the nodes in the entire domain and the grid fluxes are computed. Following this step, KATS solves the linear system, updates the temperature, and moves the mesh. The updated surface temperature, chemical state, and blowing velocity are interpolated onto the NBS centroids, while the recession vector is interpolated onto the NBS nodes. The NBS solver regenerates the near-body mesh based on the displaced surface nodes and interpolates the previous step NBS solution onto the relevant Cartesian cells. The main steps of the coupled framework are summarized in the algorithm 1.

Algorithm 1 Time integration procedure between NBS-Cart and KATS-MR solver. Start from a converged flow solution.

1: Solve governing equations on NBS grid while calling surface balance solver to converge on a new surface chemical state.
2: Interpolate NBS solution for the material solver.
3: Solve surface balance equations and compute ablation rate.
4: Interpolate surface recession to the nodes and compute grid fluxes.
5: Solve in-depth material response.
6: Move material mesh.
7: Interpolate material solution onto NBS centroids.
8: Move NBS surface nodes and regenerate near-body mesh.
9: Interpolate previous step NBS solution onto relevant Cartesian cells.
10: Solve governing equations on Cartesian grid.
11: Interpolate Cartesian solution onto NBS inflow.

The change in the coupling scheme compared to the previous studies appears in the introduction of direct coupling between the NBS and surface balance solvers. This type of coupling leads to a more accurate prediction of the surface chemical state and hence the heating. The update of the material temperature and mesh motion is not performed during the NBS-SB coupling due to the high expense of such a computation. However, as it will be shown later, the surface temperature update and recession during the NBS-SB coupling have a much lower effect on the solution accuracy as opposed to the surface chemical state. In fact, coupling in the surface balance solver allows for larger time steps to be taken on the material side, thus decreasing the overall computation time of the simulation.

5. Uncoupled - equilibrium framework

In the uncoupled approach, the heating toward the surface is modeled by the difference between the total enthalpy of the flow and the mixture enthalpy at the wall, multiplied by the heat-transfer coefficient. This form of applied heating is used when the flow conditions satisfy unity Lewis and Prandtl numbers. When the Prandtl number is not unity, the enthalpy at the boundary layer edge is represented by the recovery enthalpy. When the Lewis number is not unity, the conduction and diffusion heating by the flow are modeled by separate enthalpy potentials. This general form of the applied aerodynamic heating is implemented in KATS-MR and is shown in the equation below

$$\begin{aligned} q''_{\text{qaero}} &= \underbrace{\rho_e u_e C_h (h_{r,e} - h_{w,e})}_{\text{flow energy conduction}} + \underbrace{\rho_e u_e C_m (h_{w,e} - h_w)}_{\text{diffusion heating}} = \\ &= \underbrace{-\kappa_s \nabla T \cdot \hat{\boldsymbol{n}}}_{\substack{\text{solid energy} \\ \text{conduction}}} + \underbrace{\epsilon\sigma(T_w^4 - T_\infty^4)}_{\text{re-radiation}} + \underbrace{m''_w \left(h_w - h_{s,w}\right)}_{\text{ablation flux}}, \end{aligned} \tag{22}$$

where the first term represents the heat conducted to the surface as a result of the temperature gradient in the gas adjacent to the surface, and the second term represents the effect of endothermic and exothermic chemical reactions at the surface. The term $\rho_e u_e C_h$ is the effective heat transfer coefficient, where $\rho_e u_e$ is the boundary layer edge mass flux and C_h is the dimensionless Stanton number for heat transfer. In the enthalpy terms, $h_{r,e}$ is the recovery enthalpy at the edge of the boundary layer, $h_{w,e} = \sum_{k=1}^{ns} Y_{k,e} h_{k,w}$ is the boundary layer edge gas enthalpy frozen at the edge composition and computed at the wall temperature, and C_m is the dimensionless Stanton number for mass transfer. On the right-hand side, all terms are identical to the terms in Eq. (18), except that the ablation mass flux and wall enthalpy are evaluated based on the equilibrium conditions. It should be noted, that the wall enthalpy terms $h_{w,e}$ and h_w are easily computed with an equilibrium solver such as Mutation++ [60]. The edge composition is obtained based on the known elemental composition in the freestream and the wall composition is obtained by equilibrating the edge composition with ablating wall species. To define the conduction heat flux, the effective heat transfer coefficient can be written in the following form

$$\rho_e u_e C_h = \rho_e u_e C_{h,0} \frac{C_h}{C_{h,0}} = C_{H,0} \Omega_{\text{blw}} = C_H, \tag{23}$$

where $C_{H,0} = q''_0 / (h_{r,e} - h_w(T_0))$ is the cold wall, "unblown" heat transfer coefficient and Ω_{blw} is the blowing correction, responsible for the attenuation of the heat transfer due to the blowing of ablation products into the boundary layer. The blowing correction was developed for a Couette-type flow with transpiration at the wall, as presented in Kays et al. [61], and can be written in the following form

$$\Omega_{\text{blw}} = \frac{\Phi}{e^\Phi - 1}, \tag{24}$$

where $\Phi = 2\lambda m''_w / C_{H,0}$ and λ is an empirical, blowing reduction parameter, typically set to 0.5 for laminar flow. The recovery enthalpy in Eq. (22) is given by the following equation

$$h_{r,e} = h_e + r \frac{u_e^2}{2}, \tag{25}$$

where the first term is the boundary layer edge static enthalpy, given by $h_e = \sum_{k=1}^{ns} Y_{k,e} h_{k,e}$ and the second term is the reduced kinetic energy by a recovery factor. For a laminar boundary layer, $r \approx \sqrt{Pr}$ or approximately equal to 0.85 [62]. It should be noted, that the recovery enthalpy at the edge of the boundary layer is typically computed at the same time as the cold wall heat transfer coefficient by the flow simulation. Estimation of the boundary layer edge can be done by finding the distance from the wall where $h_e/h_0 \approx 0.99$, i.e. the local enthalpy is 1% from the total enthalpy of the flow.

To model the diffusion heating term in Eq. (22), the effective mass-transfer coefficient needs to be evaluated. The mass transfer coefficient can be related to the heat-transfer coefficient by the local Lewis number in the following form

$$\rho_e u_e C_m = C_M = C_H Le^{\gamma}, \tag{26}$$

where the exponential γ is suggested to be equal to 2/3 by Chilton and Colburn [63]. It should be noted, that for a unity Prandtl and Lewis number, the left-hand side of Eq. (22) reduces to the familiar form as shown below

$$q''_{\text{aero}} = \rho_e u_e C_h (h_{0,e} - h_w), \tag{27}$$

where $h_{0,e}$ is the total enthalpy at the edge of the boundary layer.

To close the boundary condition for the uncoupled problem, the ablation mass flux needs to be evaluated. It can be done by defining the non-dimensional ablation rate as $B'_c = m''_w/(\rho_e u_e C_m)$. With an assumption of Couette-type flow in the boundary layer and rewriting the mass balance equation (13) in terms of the elemental conservation across the boundary layer, the non-dimensional ablation rate can be written in the following form

$$B'_c = \frac{\tilde{Y}_{c,w} - \tilde{Y}_{c,e}}{1 - \tilde{Y}_{c,w}}, \tag{28}$$

where the terms $\tilde{Y}_{c,e}$ and $\tilde{Y}_{c,w}$ represent the boundary layer edge and the wall elemental mass fraction of the ablating carbon element. Following the derived non-dimensional ablation rate, the ablation rate from the material surface is given by

$$m''_w = B'_c \rho_e u_e C_m = B'_c C_M. \tag{29}$$

6. Results and discussion

The coupled framework between the CHAMPS NBS-Cart and KATS-MR solvers is applied to study the ablation of graphite using two experimental test cases. In both cases, the problem is modeled as a two-dimensional axisymmetric slice at zero angle of attack. The flow wall spacing is set to 5×10^{-7} m based on the performed grid convergence study shown in Fig. 20 in Appendix C. The material wall spacing is set to 1×10^{-6} m. The NBS-Cart solver uses an unsteady implicit method with dual time stepping which allows for relatively large time steps to be taken on the fluid side, on the order of 1×10^{-4} s. On the other hand, the KATS-MR solver uses the backward Euler implicit time stepping to advance the material solution with a time step set to 6×10^{-3} s throughout the simulation. During the coupled interaction, flow convergence on the new wall state is typically achieved by reducing the residual 2–3 orders of magnitude within the preset 200 sub-step operations. The difference in timescale between the flow and material physics permits using a lower time step size on the fluid side since the fluid time step is quite large relative to the local timescale. This ensures sufficient convergence of the boundary layer during the coupled interaction with the material solver.

Finally, the simulation of both test cases is performed with the assumption that the samples are inserted into the arc-jet stream with a certain delay caused by the motion of the sting. This delay leads to a transient increase in the heat flux and pressure on the sample surface which affects the material performance, especially in the short-duration experiments [64]. In this study, a 0.35 s heat flux linear ramping was applied, which increases from the value of zero to the nominal conditions. The sample extraction from the jet is modeled by linearly damping the heat flux over the same 0.35 s interval. The pressure ramping was not applied in the cases.

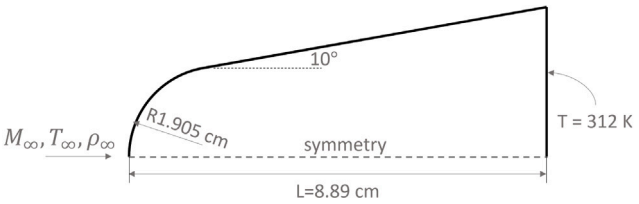

Fig. 4. Case 1 — sphere-cone model.

6.1. Case 1 — sphere cone model

The first test case is a sphere cone graphite model tested in the IHF arc-jet facility at NASA Ames Research Center [28,29]. As reported in the reference studies, the estimated total enthalpy in this test is 27 MJ/kg, with a stagnation point heat flux of 2100 W/cm^2, and a stagnation point pressure of 0.80 atm. At these high enthalpy conditions, nitrogen gas is partially dissociated and oxygen is fully dissociated. The geometry of the model is a 10° half-angle sphere cone with a nose radius of 1.905 cm and length of 8.89 cm as shown in Fig. 4. The back face of the model is connected to a water-cooled holder and the wall temperature is assumed to remain at 312 K. The material is Poco graphite, with properties extracted from the work of Minyushkin and Kryukov [48] and a solid density of 1730 kg/m^3. The flow conditions, extracted upstream of the shock were obtained from Ref. [28] and are shown in Table 1. The reported total duration of the experiment is 30 s The diagnostics of this test case included pyrometer and infrared camera measurement at 45° location, as well as the measurement of recession at 0° and 45° locations.

A visualization of the flow field and material temperature at 0 and 30 s is shown in Fig. 5 on separate scales for flow and material domains. The surface temperature at the nose-cone exceeds 3000 K, leading to a strong sublimation regime and a significant amount of recession and displacement of the shock layer.

To compare the coupled results and experiment with the uncoupled approach, a flow solution on a non-catalytic, cold wall was obtained for the initial and final shape of the geometry predicted by the coupled simulation. This is done to account for the considerable shape change effect on the film coefficients. Figs. 6(a) and 6(b) show the normalized heat flux and pressure profiles, where the solid line represents the solution on the initial geometry and the dashed lines relate to the final shape. Both profiles were normalized by the stagnation point value shown in the figures in the legend. The simulations were performed using Lewis number 1.4 and 1.0, however, the profiles are shown only for the Lewis number 1.0. It can be seen from Fig. 6(a) that the shape change leads to an approximately 10% decrease in the cold wall heat flux at the stagnation point. The 10% decrease in the heat flux translates directly to the 10% decrease in the heat and mass-transfer coefficients, affecting the heating and ablation rate of the material. Away from the stagnation point, toward the 45° the heat flux slightly increases and then decreases again close to the transition to the conical part of the geometry. The pressure profile in Fig. 6(b) shows only a slight change away from the stagnation region on the nose section. This amount of pressure change is not expected to lead to any significant effect on the material response. The stagnation point heating, obtained with Le = 1.0, is equal to 1768.6 W/cm^2, which is considerably lower than the reported value of 2100 W/cm^2 in the experiment. With Lewis number Le = 1.4 the heat flux grows to 1923 W/cm^2, which is still below the experimental value. Noting that both simulations were

Table 1
Freestream conditions upstream of the shock for test case 1, obtained from Ref. [28].

Property	u_∞ (m/s)	ρ_∞ (kg/m^3)	T_{tr} (K)	T_v (K)	Y_{N_2}	Y_{O_2}	Y_{NO}	Y_N	Y_O
Value	5354	0.003	1428	1428	0.6169	0.0	0.0046	0.1212	0.2573

Table 2
Aerodynamic heating parameters for case 1.

Condition	$C_{H,0}$ (kg/m^2-s)	h_r (MJ/kg)	p_w (kPa)
Le = 1.4	0.8264	23.88	79.62
Le = 1.0	0.7606	23.88	79.75

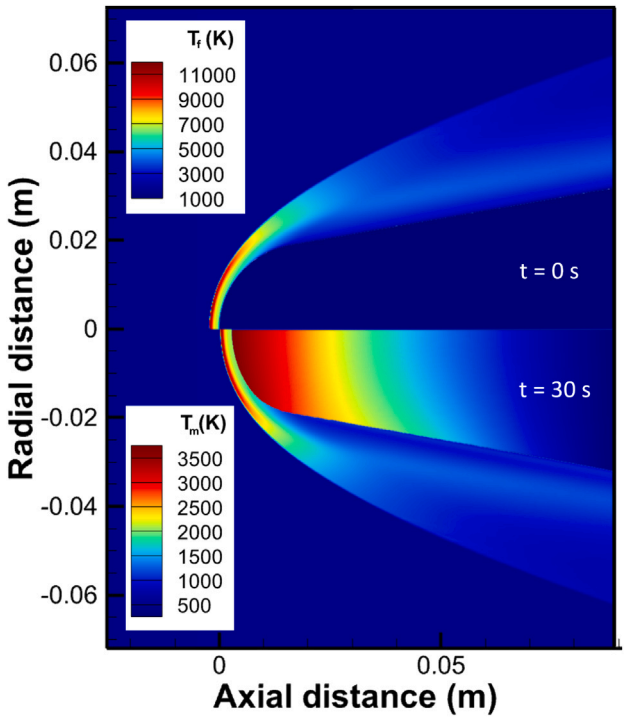

Fig. 5. Case 1 — flow and material temperature contours at 0 and 30 s (on different scales).

performed with non-catalytic wall conditions can explain the under-prediction of the experimental value. Heat flux measurement probes are typically made of copper, which is known to be catalytic to the incoming atomic species, however, the choice of a non-catalytic wall for graphite surface was based on the performed simulations, showing that the fully catalytic assumption, at least in the current studies, is too conservative. The predicted stagnation point pressure of 79.75 kPa matches closely the experimental value of 0.8 atm.

Based on the obtained heat flux profiles, the film coefficient is computed and shown along with other quantities in Table 2. The "unblown" wall heat transfer coefficient was estimated based on the cold wall heat flux and recovery enthalpy extracted at the boundary layer edge at the stagnation point. The wall enthalpy was computed based on the equilibrium air composition at the wall. During the ablation simulation, the edge and wall enthalpies are calculated with Mutation++.

The next set of figures shows the comparison of the predicted results to the experimental measurements. The numerical simulations are performed with coupled, finite-rate (FR) and uncoupled, equilibrium (EQ) approaches using the assumption of Lewis number of 1.4 and 1.0. Fig. 7(a) shows the predicted surface temperature history at 45° location relative to the stagnation point. The finite-rate results with Le = 1.4 and Le = 1.0 overestimate the measured temperature obtained with the pyrometer and IR camera, predicting approximately 200 K (Le = 1.4) and 100 K (Le = 1.0) higher temperature at the end of the simulation. On the contrary, the equilibrium simulation predicts close agreement with the experimental data throughout the whole duration of the measurement. It is apparent that the higher temperatures predicted with Le = 1.4 are directly related to the effect of the Lewis number on diffusion heating in both approaches. Fig. 7(b) shows the distribution of the surface temperature at t = 30 s. The finite-rate chemistry predicts higher temperature in the leading portion of the nose region, however downstream the nose and especially at the flank, the predicted temperature with Le = 1.0 closely aligns with the IR measurement. The uncoupled, equilibrium approach, on the contrary, predicts closer agreement with the experimental data at the upper nose section but significantly deviates downstream. The deviation is obviously caused by the under-predicted heating in this region which could be related to several factors. As a reminder, the heat-transfer coefficient in the uncoupled approach was computed based on the non-catalytic wall condition which results in the lower heating to the surface. This can explain the lower temperature predicted downstream of the nose. However, assuming a fully catalytic wall would increase the heating not only downstream, but also at the stagnation region, leading to a stronger overprediction of temperature at the nose. The second potential reason for the deviation could be related to the inaccurate estimation of the evolution of the heat- and mass-transfer coefficients using the blowing correction. In this case, the lower heating could be caused by the too strong reduction of the heat flux by the blowing correlation. Finally, it is known that local chemical conditions start to deviate from equilibrium downstream of the stagnation region. Deviation from the equilibrium would change the surface chemical composition and affect the wall enthalpy that controls the heating to the surface. Apparently, multiple factors could affect the performance of the uncoupled approach, depending on the region of the geometry. Further analysis of the problem is left for future studies, however, some insight into the factors affecting the accuracy of the uncoupled approach can be derived from our recent work exploring the ablation of camphor at hypersonic conditions [24].

The predicted amount of recession at 0° and 45° locations is shown in Fig. 8(a). It can be seen that both finite-rate and equilibrium approaches predict very close agreement with the measured data at the stagnation point with Le = 1.0. At 45° the equilibrium approach under-predicts the amount of recession compared to the finite-rate data, which matches perfectly the measurement. Typically, away from the stagnation point, non-equilibrium conditions develop along the geometry, which would lead to the overestimation of the non-dimensional ablation rate by the equilibrium solver. However, in the figure, we see an underestimation of the ablation rate, which is linked to the inaccurate estimation of the mass-transfer coefficient away from the stagnation region. With the assumption of Le = 1.4 both approaches strongly over-predict the measurement, showing stronger deviation at the stagnation point. The direct reason for the overprediction at the higher Lewis number is the strong effect of the diffusion coefficient on the ablation rate. In addition, since both locations reach a sublimation regime, the higher diffusion heat flux resulting from a higher Lewis number leads to a higher temperature rise and hence, a higher sublimation rate. An additional comparison of the ablation prediction by the finite-rate and equilibrium approaches is shown in Fig. 8(b) where the ablation mass flux is plotted along the surface. The two experimental points shown in the figure were likely extracted by the original authors based on the recession rate extracted from the previous figure multiplied by the material density. The figure shows a snapshot of the material ablation rate at the end of the simulation pointing at the comparative performance of the two approaches. Away from the stagnation point the equilibrium approach under-performs the finite-rate one, while at the

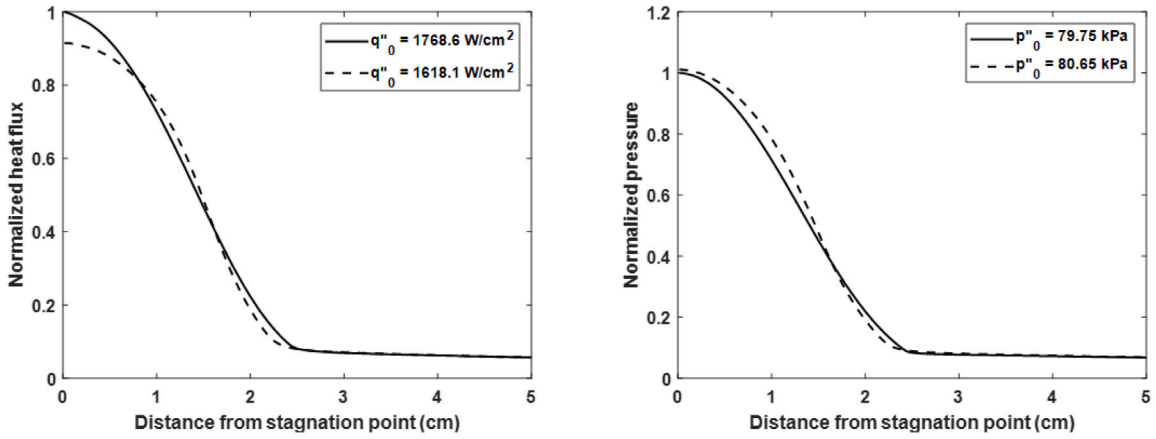

(a) Heat flux. (b) Pressure.

Fig. 6. Case 1 — normalized cold wall heat flux and pressure profiles, predicted at initial (solid lines) and final geometry (dashed lines) shapes (T_{wall} = 312 K, Le = 1.0, non-catalytic wall).

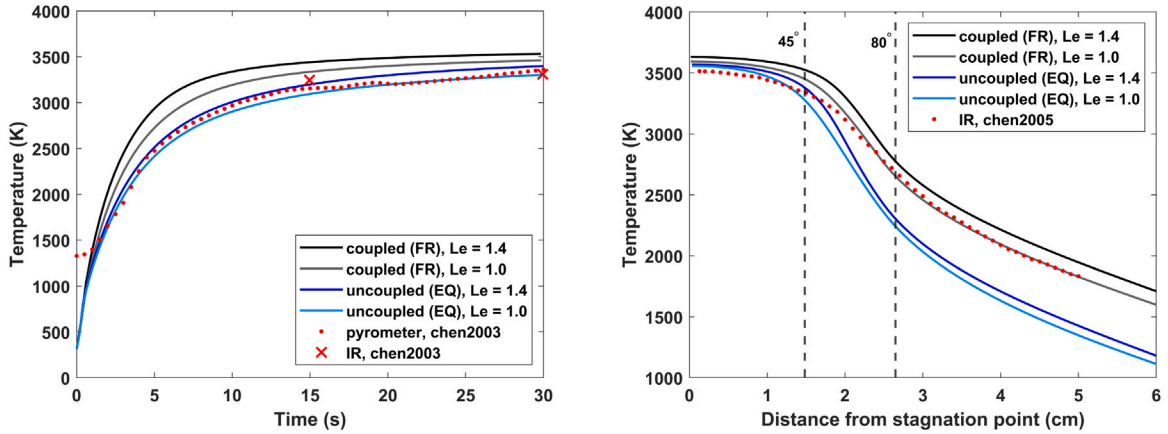

(a) Surface temperature history at 45° relative to stagnation point. (b) Surface temperature distribution at t = 30 sec.

Fig. 7. Case 1 — comparison of predicted and measured surface temperature with coupled (finite-rate) and uncoupled (equilibrium) models.

stagnation point, both models predict an almost identical ablation rate with Le = 1.0. The assumption of Le = 1.4 leads to the deviation of two approaches also at the stagnation point. The difference is potentially related to the relation between the mass- and heat-transfer coefficients shown in Eq. (26). For the non-unity Lewis number, the relationship between the two coefficients depends on the exponent value, which might be too high for the current case.

As it was presented earlier in Section 4.3, the new coupling scheme between the solvers, where the NBS interacts directly with the surface balance solver, provides a way to use larger material time steps. Figs. 9(a) and 9(b) show the sensitivity study results where the material time step is increased from 1.2×10^{-3} s to 1.2×10^{-2} s, by preserving all other simulation parameters, such as the fluid step and the convergence criteria. The results show normalized temperature and ablation mass flux time histories at 0° and 45° locations. The results are shown for the first 15 s of the simulation. The normalization of the curves was performed by the highest predicted value in the most refined time step case. It can be seen, that increasing the material step by a factor of 10, only slightly affects the accuracy of the solution despite the strong temperature gradients present at the wall in this high-heating case. The temperature curves are almost identical at both locations, while the ablation mass flux shows a slight deviation at higher rates entering the sublimation regime. It can also be seen, that as a general tendency, the increase of the material time step leads to a decrease in the predicted surface temperature and ablation rate. This effect is, however, relatively small even in the largest material step and can be tolerated as it leads to a significantly lower computational cost for the simulation.

6.2. Case 2 — iso-q model

The second test case studied in this work is an iso-q graphite model tested in an air environment with the addition of argon gas in the IHF arc-jet facility at NASA Ames using the 6″ nozzle [65]. The test consisted of two arc-jet runs at identical conditions and material setups, but different duration, with the first run lasting 5.8 s and the second lasting 10.8 s In this work, only the shorter duration case is presented, however, both cases were analyzed and studied, showing similar results. The estimated total enthalpy in this case, is 20.7 MJ/kg, with a stagnation point heat flux of 1306 W/cm^2 and a stagnation pressure of 127.3 kPa, measured with a 4-inch in diameter hemisphere coaxial calorimeter. The geometry of the graphite sample is a 4-inch in diameter iso-q model mounted on top of LI2200 insulator as shown in Fig. 10. The measurement in this test included a series of one- and two-color pyrometers pointing at the stagnation point and a thermocouple (TC) plug with five thermocouples at different depths as shown in Fig. 10(a). The arc-jet simulation was performed with the DPLR code [7] by setting the plenum inflow conditions based

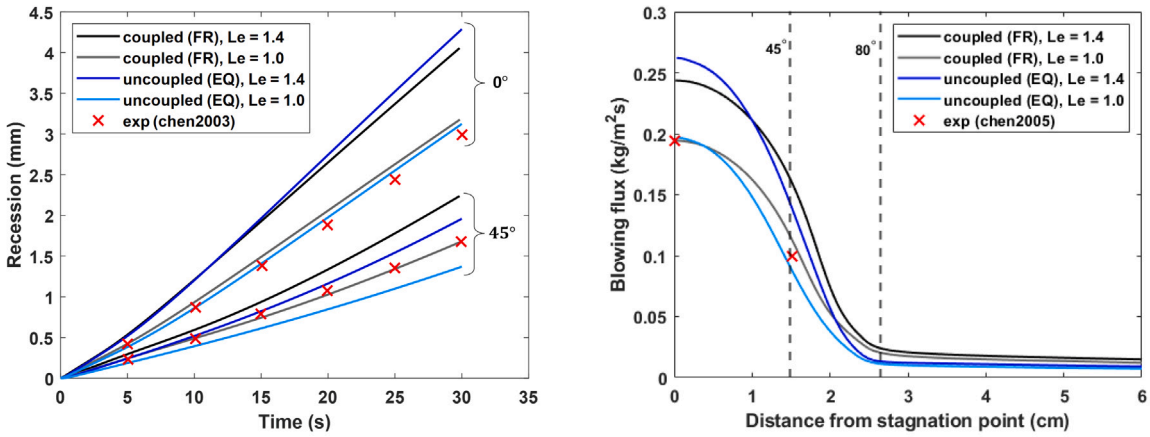

(a) Surface recession history at 0° and 45° locations. (b) Distribution of surface mass blowing at t = 30 sec.

Fig. 8. Case 1 — comparison of the predicted and measured surface recession and mass loss flux with coupled (finite-rate) and uncoupled (equilibrium) models.

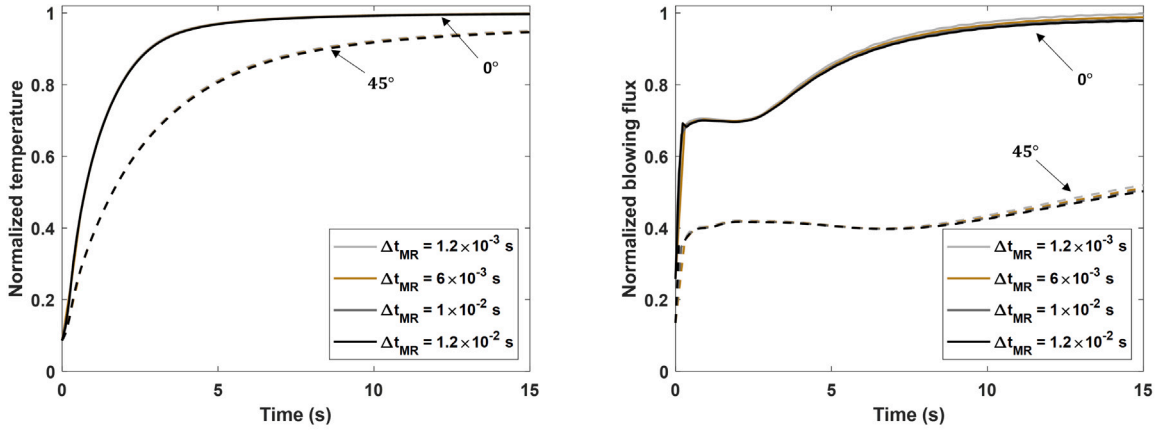

(a) Normalized surface temperature history. (b) Normalized surface mass blowing history.

Fig. 9. Case 1 — Effect of incremental material time step on solution accuracy in the implemented coupling scheme.

Table 3
Nozzle plenum and freestream conditions for case 2.

Property	u_∞ (m/s)	ρ_∞ (kg/m^3)	T_{tr} (K)	T_v (K)	Y_{N_2}	Y_{O_2}	Y_{NO}	Y_N	Y_O	Y_{Ar}
Plenum	273.54	0.26987	7331.11	7331.11	0.491291	0.000357	0.012702	0.210864	0.209842	0.074944
Freestream	4327.4	0.00763	3812.44	4035.04	0.6317	3.0191×10^{-5}	4.437×10^{-4}	0.07617	0.2167	0.074944

on the estimated total enthalpy and measured pressure and mass flow rates of the oxygen, nitrogen, and argon gases. The flow conditions for the CHAMPS-KATS coupled study were set by sampling the freestream condition on the axis upstream of the shock. Table 3 summarizes the arc-jet plenum conditions and the extracted freestream conditions. The suggested material in this test case is ultra-fine Poco graphite, where the thermal properties were obtained from Sheppard et al. [47] and the density was assumed to equal 1660 kg/m^3. The thermal and physical properties of LI2200 insulator were obtained from Refs. [66,67].

The coupled simulations were performed with the assembly of the graphite coupon on top of the insulator and compared to the pure coupon case. It was assumed that the coupon and the insulator were in full contact at the interface, disregarding the air gap as shown in Fig. 11. The back wall of the insulator was assumed adiabatic. The initial temperature of the materials was set to 293.15 K based on the TC measurement prior to the heating phase. Two types of boundary conditions were set along the surface. The graphite boundary was set identically to the previous case with applied conduction and diffusion heating, chemical reactions based on the ACA model, and recession. The insulator surface was set to be non-catalytic (NC), enforcing zero diffusion heat flux at the wall and non-recessing. Due to the short duration of the run, the transient insertion and extraction of the sting are expected to have a sensible effect on the material thermal response and similarly to the previous case, a 0.35 s linear ramping and damping interval was applied on the heat flux profile at the beginning and at the end of the heating phase. The actual steady heating phase, due to the transients lasted 5.1 s Following the extraction of the sample from the jet, the material was allowed to cool down by re-radiation until the end of the simulation at t = 20 s.

Simulating material response based on the freestream conditions extracted upstream of the shock may introduce inaccuracies due to the jet divergence exiting the nozzle and other factors. Fig. 12 shows the comparison between the normalized heat flux and pressure profiles obtained from the full arc-jet simulation with DPLR and from the freestream simulation performed by CHAMPS. The heat flux and pressure profiles were normalized by the stagnation value shown in the figures in the legend. The arc-jet simulation was performed with the assumption of a fully catalytic (FC) surface and a wall temperature of

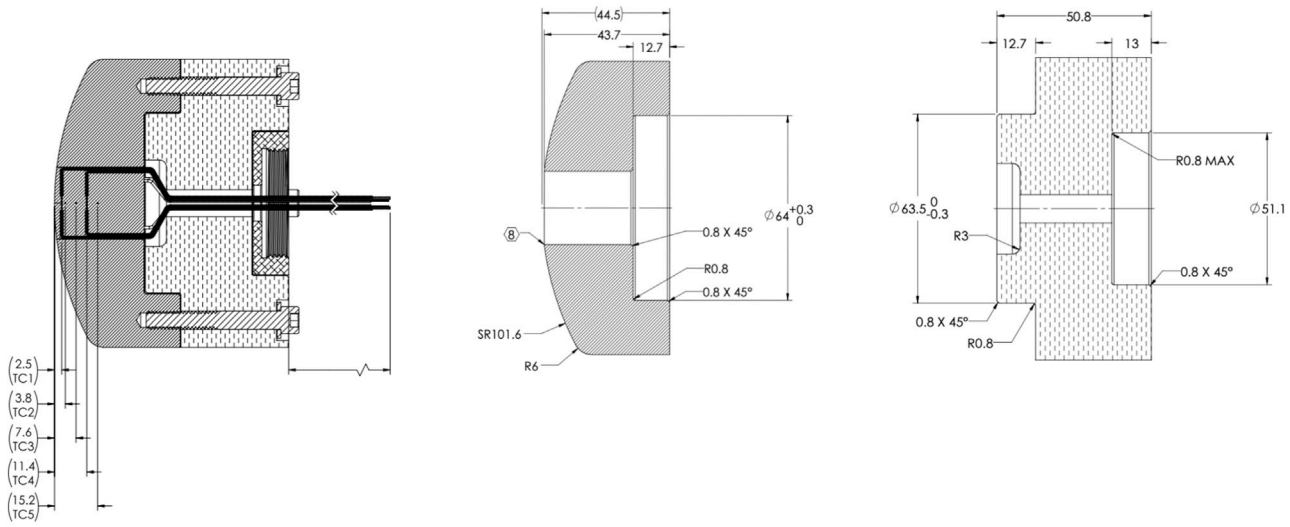

(a) Ablator with TC plug and insulator. (b) Ablator, Poco graphite. (c) Insulator, LI2200.

Fig. 10. Case 2 — assembly of iso-q coupon with TC plug mounted on top of insulator.

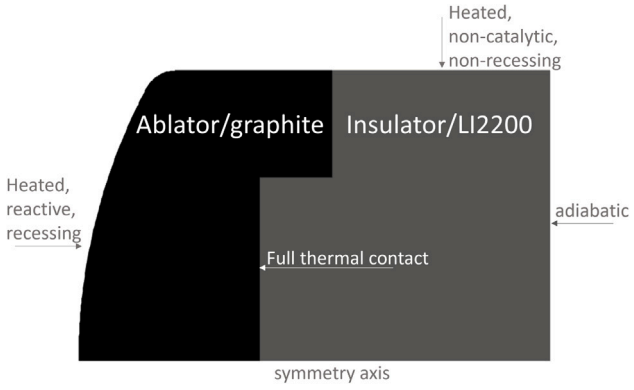

Fig. 11. Case 2 — axisymmetric computational model of ablator and insulator assembly.

500 K, set to represent the conditions at the copper calorimeter surface. The CHAMPS simulation was performed for graphite, assuming a non-catalytic (NC) surface and an initial temperature of the material at 293.15 K, obtained from thermocouples. The non-catalytic assumption was explained earlier and is related to the experience gained in simulating graphite test cases. The Lewis number in the CHAMPS simulation was set to 1.4. First, the predicted fully catalytic flux, reported at the stagnation point in the legend, is higher than the non-catalytic one. This fact indicates that the flow is dissociated past the shock layer and recombination at the surface increases the diffusion heating. It can be seen from the figure that a slight difference exists in the shape of the profiles. The difference in the heat flux profile in Fig. 12(a) appears mostly in the shoulder region, where the fully catalytic assumption predicts a higher spike due to local recombination. The slight difference in the pressure profiles in Fig. 12(b) points to the effect of jet divergence. The assumption of the uniform inflow as in the freestream simulation leads to a slightly thicker pressure profile, which increases away from the stagnation point and stays slightly higher at the side of the sample. Overall, the assumption of the uniform inflow conditions extracted from the arc-jet simulation appears to be reasonably accurate.

The aerodynamic heating parameters extracted for the uncoupled simulations are given in Table 4. The cold wall heat transfer coefficient

Table 4
Aerodynamic heating parameters for case 2.

Condition	$C_{H,0}$ (kg/m^2-s)	h_r (MJ/kg)	p_w (kPa)
Le = 1.4	0.5258	19.71	140.516
Le = 1.0	0.4729	19.71	140.502

is estimated similarly to the previous case based on the recovery enthalpy and equilibrium air plus argon enthalpy at the wall conditions.

Fig. 13 shows a visualization of the temperature in the flow and material domains, plotted at the beginning of the simulation and at the end of the heating pulse at 5.45 s It can be seen that by the end of the heating phase, a significant amount of heat penetrates into the graphite material, while most of the insulator stays close to the initial temperature. The insulator develops a distinct temperature rise in the near-surface region due to the low conductivity of the material. A similar behavior of the insulator temperature rise can be observed in the work of Gokcen et al. [4]. Due to the short duration of the test, the measured material recession is limited to around 0.1 mm at the stagnation point and no significant shape change of the material is observed.

The measured temperature from the thermocouples is first used to perform a one-dimensional TC-driver simulation to estimate the accuracy of the implemented material properties. In the TC-driver approach, the measured temperature from the first shallow TC is used as a boundary condition in the material simulation. The material length is reduced accordingly, and an adiabatic condition is applied at the back wall. Fig. 14 shows the predicted in-depth temperatures and a comparison to the thermocouples. The two shallow TCs closely match the experimental data and a slight overestimation is seen at the two deeper locations. Given that the TC-driver approach is performed on a 1D geometry, the simulation does not consider the potential lateral flow of heat into the centerline region. Since graphite is a highly conductive material, some heat from the side wall may augment the centerline temperature. Under these conditions, if the material properties are accurate, the TC-driver approach would actually predict lower temperatures at the deeper locations compared to the measurement. Based on that, the over-prediction of the TC data indicates that the material thermal properties might be inaccurate. The next set of figures presents

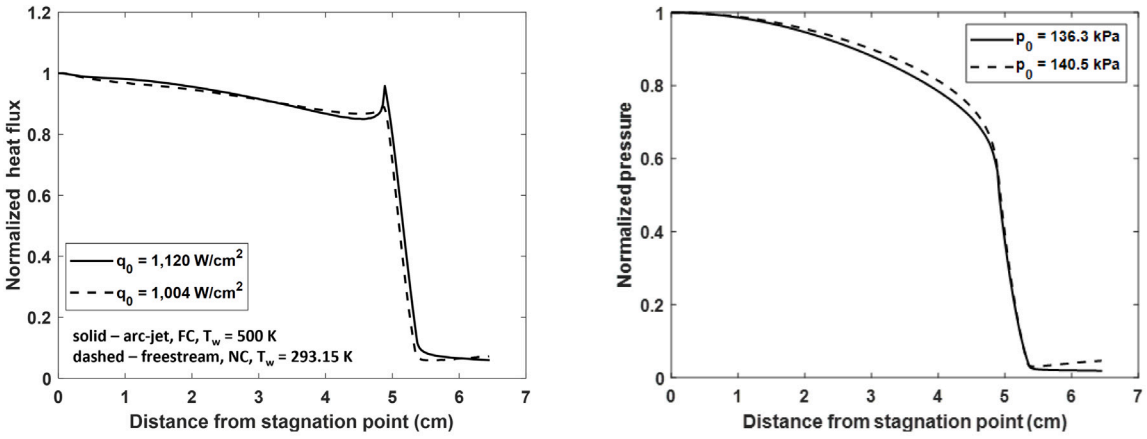

(a) Heat flux. (b) Pressure.

Fig. 12. Normalized cold wall heat flux and pressure profiles, predicted with full arc-jet simulation and based on the freestream conditions extracted upstream of the shock (Le = 1.4).

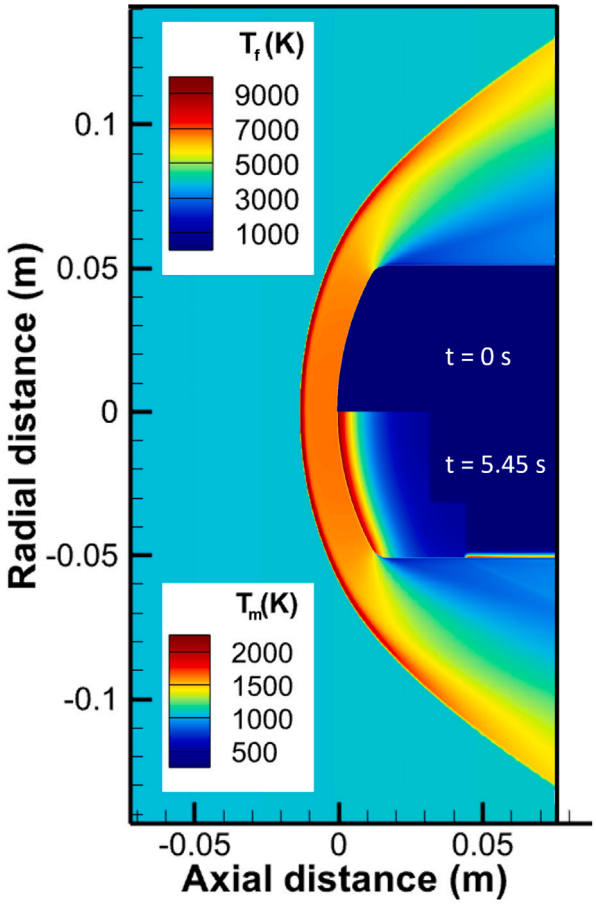

Fig. 13. Case 2 — flow and material temperature contours at the beginning and at the end of the heating phase.

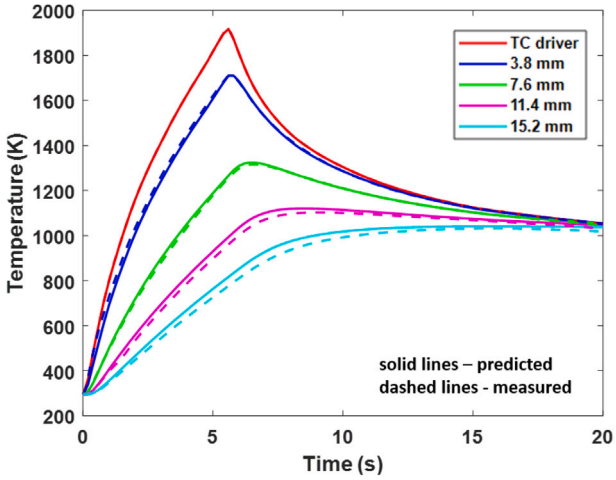

Fig. 14. In-depth temperature histories predicted with TC-driver approach.

the results from the coupled and uncoupled simulations and explores the effect of different uncertainties on the solution accuracy.

Fig. 15(a) shows the comparison of the predicted surface temperature distribution with the data from the IR camera, extracted at t = 5.0 s. The predicted data is shown from the coupled (finite-rate) and uncoupled (equilibrium) approaches, simulated using Le = 1.4 and Le = 1.0. The IR measurement was performed based on the assumption of surface emissivity of 1. In the presented data, the measurement was corrected for the emissivity of ultra-fine graphite, using the emissivity data from Eq. (12). Observing the results, we first see that both approaches align very well between themselves along the front surface of the geometry and deviate toward the shoulder and the side wall. Similarly to the previous test case, the lower predicted temperature in the uncoupled approach can be related to the deviation from equilibrium and the decreased accuracy of the film coefficient approach away from the stagnation region. Comparing the predictions to the experimental IR data, we see that the assumption of Le = 1.4 leads to the closest agreement with the measurement, showing a slight overestimation toward the shoulder.

Performing the comparison with the measured recession (0.1 mm) is somewhat tricky in this case, due to the very small amount of recession and the lack of uncertainty data. For the sack of any future discussions, the coupled simulations predict stagnation point recession of 0.25 mm and 0.3 mm for the Le = 1.0 and Le = 1.4 cases, overestimating the given experimental value by a significant factor. If comparing the amount of recession in the longer duration case (10.8 s), the given experimental value is 0.7 mm, while the coupled simulation with Le = 1.4 predicts 0.56 mm, thus under-predicting the measurement. A quantitative comparison of the mass loss flux between the coupled and uncoupled approaches is shown in Fig. 15(b), extracted at t = 5.0 s for consistency. With the assumption of Le = 1.0 the mass loss fluxes of

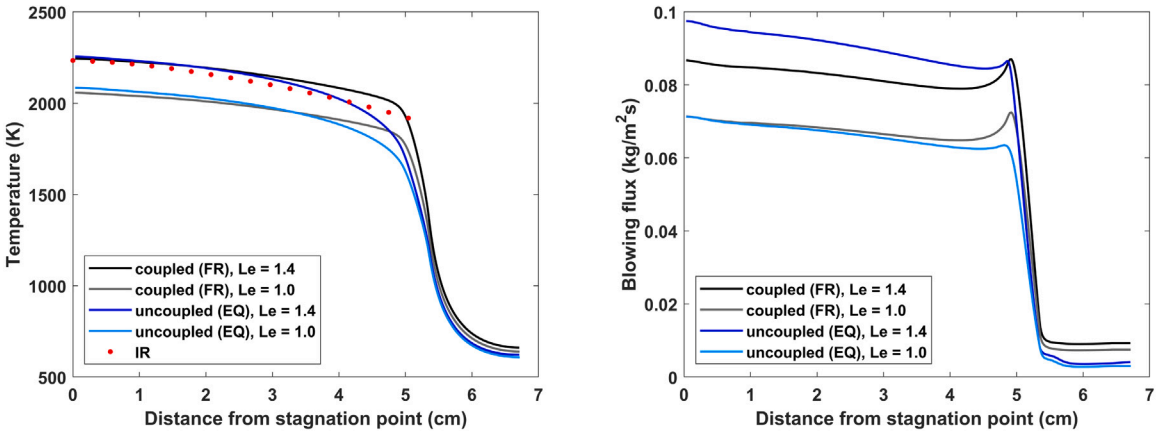

(a) Surface temperature. (b) Surface mass loss flux.

Fig. 15. Comparison of the predicted distribution of surface temperature and mass loss flux using finite-rate (coupled) and equilibrium (uncoupled) approaches. The data is extracted at t = 5.0 s.

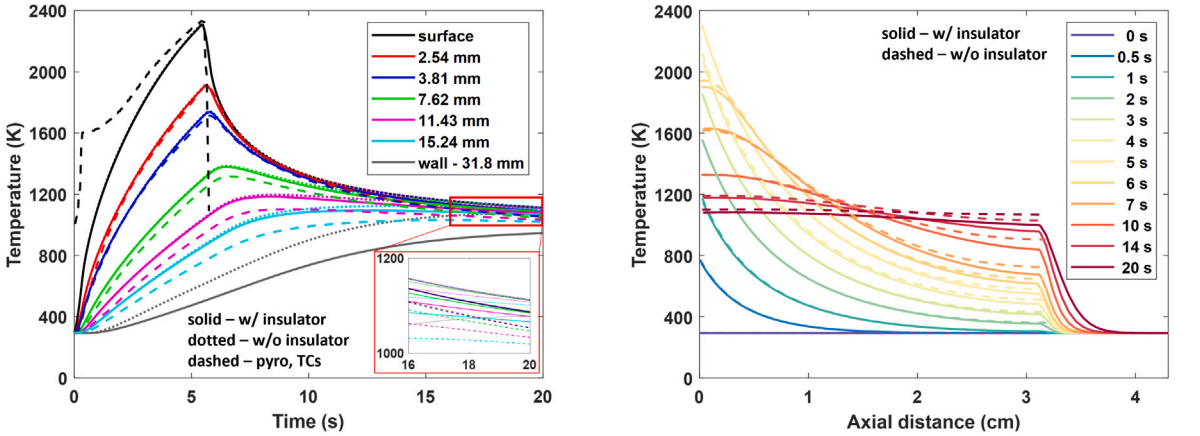

(a) Predicted temperature histories in the pure ablator and assembly cases (Le = 1.4).

(b) Distribution on in-depth temperatures along axis in graphite and in graphite with insulator cases.

Fig. 16. Case 2 — effect of insulator on temperature prediction with coupled approach.

the two approaches agree extremely well along the front portion of the geometry, and deviate toward the shoulder and the side wall, similar to the temperature profile in the previous figure. The assumption of Le = 1.4, however, leads to a considerable overprediction by the uncoupled approach along the front surface. The peaks at the shoulder match relatively well, with some minor spatial misalignment for unclear reasons. At the side wall, the uncoupled approach consistently predicts lower mass flux. The higher predicted values at the front surface can be linked to the overestimation of the mass-transfer coefficient with the Chilton-Colburn correlation in Eq. (26). The reason for the lower values at the side wall is harder to analyze as the prediction is affected by multiple factors, such as local non-equilibrium and the decreased accuracy of the film coefficient approach. Finally, the apparent inconsistency between the close alignment of the stagnation region temperature in Fig. 15(a) and the misalignment of the mass loss flux in Fig. 15(b) in the Le = 1.4 case is explained by the fact that the ablation heat flux has a relatively small contribution to the overall energy balance at the surface in the current case and hence, barely affects the material temperature.

Fig. 16(a) shows the comparison of the predicted temperatures performed with the coupled approach using Le = 1.4 to the measurement by the pyrometer and in-depth thermocouples. The figure includes the results from the full assembly of the ablator and the insulator, marked with solid lines, and results from the pure ablator case with an adiabatic back wall condition, marked with dotted lines. As mentioned earlier, the experiment included multiple one- and two-color pyrometers pointing at the stagnation point. The two-color pyrometers experienced a strong overshoot in the first 3 s of the experiment and this data is not shown, and only two one-color pyrometers showed a consistent measurement. The temperature from these two pyrometers was averaged and corrected for the surface emissivity of graphite and is shown with a dashed black curve in the figure. The accuracy of the transient pyrometer measurement raises additional concerns due to the initially high-temperature jump, which seems to be inconsistent with the shallow TCs response. The potential reason for this behavior could be a strong emission from the dissociated species in the shock layer that overcomes the emission from the graphite surface at the initial low temperature of the material. The predicted surface temperature appears to reach the pyrometer reading only by the end of the heating phase. The in-depth temperatures follow closely the shallow TCs but overestimate at the deeper locations. In fact, the deviation appears to grow both in-depth and with increasing material temperature. During the cool-down phase and by the end of the simulation, as shown in the zoomed-in window, the material temperature stays above the TC readings. Comparing the predicted temperatures between the two material setups shows a negligible effect of the insulator on the in-depth temperature predictions. The presence of the insulator appears to decrease the graphite temperature during the cooling phase, as

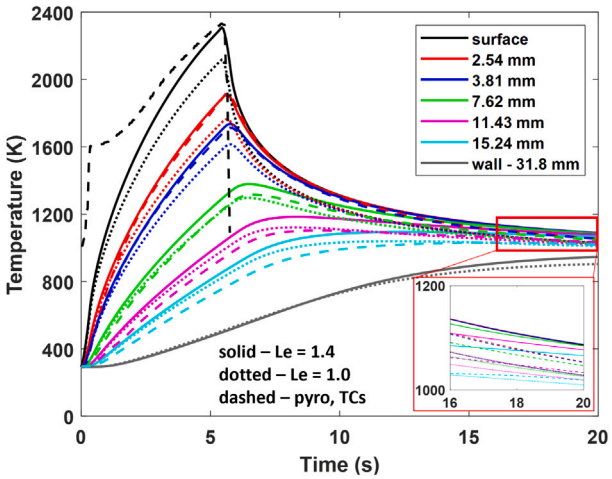

Fig. 17. Case 2 — effect of Lewis number on temperature prediction with coupled approach (w/insulator).

some amount of heat is soaked back into the relatively cold insulator structure.

The effect of the insulator on the thermal response is shown in Fig. 16(b), where a series of time snapshots of temperature distribution extracted along the axis is shown for two material setups. The presence of the insulator affects the graphite temperature only in the very vicinity of the back wall, and for the majority of the bulk material, the temperatures in the two cases closely align. The adiabatic wall condition at the graphite back wall proves to be an accurate assumption if the region of interest lies further away from the back wall.

Overestimation of temperatures at the deeper locations appears not to be linked to the effect of the insulator. The fact that at the shallow locations, the temperatures are well predicted and at the deeper locations the deviation increasingly grows could point to the inaccurate thermal properties of the material. This fact alone, though, cannot improve the prediction as the decrease in the material thermal diffusivity, for example, would limit the flow of heat into the deeper portion of the material, but in turn, would increase the near-surface temperatures. The heating environment is another potential factor that could affect the material thermal response. For example, uncertainty in the estimated arc-jet conditions, such as total enthalpy, is one of the factors that could affect the surface heating rates. Another factor is the transport properties of the flow that dictate the rate of conduction and diffusion heat fluxes toward the material. To build an intuition in this problem, we explore first the effect of the Lewis number on the material thermal response. Fig. 17 shows a comparison between two simulations with Le = 1.4 and Le = 1.0. The decrease in the Lewis number leads to a significant decrease in the material temperature due to the decrease in diffusive heating. The surface and two shallow TCs temperatures are strongly under-predicted, while the prediction in deeper locations is improved. Interestingly though, despite the significant decrease of the material heating the temperature at the two deepest locations is still overpredicted.

Overestimation of the in-depth temperatures aligns with the earlier observation in the TC-driver approach and implies that the material thermal diffusivity tends to be over-estimated. The factors that affect thermal diffusivity are specific heat, conductivity, and density. The specific heat of different types of Poco graphites is very similar as can be seen in Fig. 2(b) and as mentioned in Ref. [47]. Conductivity has a stronger variation between different grades of Poco graphite and has a strong temperature dependence. The conductivity of fine-grade graphite, for example, is approximately 10% lower than the ultra-fine grade graphite suggested for this study and somewhat comparable to the conductivity provided by Touloukian et al. [44]. The effect of density variation is also substantial and would lead to a shift in the predicted temperatures. In this work, we explore the effect of conductivity on the material thermal response prediction. Assuming Le = 1.0, we run two additional cases. In the first case, shown in Fig. 18(a), a conductivity of fine-grade graphite is used and compared to the ultra-fine one. The temperature in the shallow region has increased and in the deeper locations has slightly decreased, confirming the intuition. The deviation from the measured data is still high. The effect of the further decrease in the conductivity is shown in Fig. 18(b), where the conductivity of fine-grade graphite is artificially decreased by 10%. In this case, the temperature in the three deepest locations is accurately matching the measurements, while the temperature of the two shallow TCs and surface is still slightly under-predicted.

Apparently, multiple uncertainties at once affect the accuracy of the material thermal response prediction. Factors such as surface emissivity, have a relatively low effect in the current case. Manufacturing factors, such as potential thermal resistance across the TC plug or suction of heat by the metallic bolts used to connect the assembly have additional but secondary-level effects. Bad thermal contact between the thermocouple tips and the material is ruled away in this study based on the comparison of the TC readings with the longer duration run. The thermocouple readings showed almost identical temperature rise between the two runs, especially at the deeper locations.

To summarize the significant effects of the environmental and material uncertainties Fig. 19 shows the computed Mean Signed Deviation (MSD) between the predicted in-depth temperatures and the thermocouples. The surface temperature is not included in the evaluation due to the strong discrepancy with the measured data. The horizontal axis in the figure lists the different uncertainty scenarios, listed as cases, numbered from 1 to 6, and each vertical bar in the case represents the MSD from the given thermocouple. The colors of the bars correspond to the colors of the curves in the previous figures. The cases in the figure are ordered based on the Mean Squared Error (MSE), averaged over five thermocouples. The summary of the analyzed cases is given in Table 5, where the MSD and MSE columns represent the averaged quantities over five thermocouples. The highest error corresponds to the case that simulated pure ablator without the insulator and using Le = 1.4 and ultra-fine graphite properties. Remarkably, the lowest error corresponds to the combination of the Lewis number reduction and decrease in the material conductivity.

Overall, by comparing the results from the two test cases we observe some inconsistency in the predictions. The observed agreement with the IR measurement predicted in the iso-q case with Le = 1.4 is somewhat inconsistent with the sphere-cone case, where the assumption of Le = 1.4 leads to a strong overestimation of the surface temperature and recession. One difference between the two cases appears in the implemented material properties, where the conductivity and density of the material are higher in the sphere-cone case. However, the conductivity and density have an opposite effect on the thermal diffusivity, somewhat compensating for the properties difference effect. Another particular difference between the two cases appears in the heat flux conditions that cause strong sublimation at the nose in the sphere-cone case and lead only to an oxidation regime in the iso-q case. The additional chemical reactions involved in the sublimation regime lead to a different chemical composition at the surface that affects the diffusive heating and transport properties. In addition, the use of the constant Lewis number approach to estimate the diffusion coefficient introduces another source of uncertainty. It is likely a case that species do not have identical diffusion coefficients and hence, estimating the environment by a single effective diffusion coefficient may lead to the wrong estimation of the individual diffusive heat fluxes. It is hard to point exactly at the reason for the discrepancy between the cases, but modeling the diffusion with a higher fidelity model could rule out some of the uncertainties. Additionally, conducting experiments with a higher heat flux for the iso-q case could shed more light on the performance of the models in the sublimation regime.

Table 5
Uncertainty scenarios affecting material thermal response. MSD and MSE values are the averaged quantities over five thermocouples.

Case	Description	MSD (K)	MSE (K)
1	ultra-fine grade, Le = 1.4, w/o insulator.	57.3	61.26
2	ultra-fine grade, Le = 1.4, w/insulator.	42.79	46.92
3	ultra-fine grade, Le = 1.0, w/insulator.	−18.52	46.68
4	fine grade, Le = 1.0, w/insulator.	−13.01	31.83
5	fine grade, conductivity at 90%, Le = 1.0, w/insulator.	−10.4	20.29

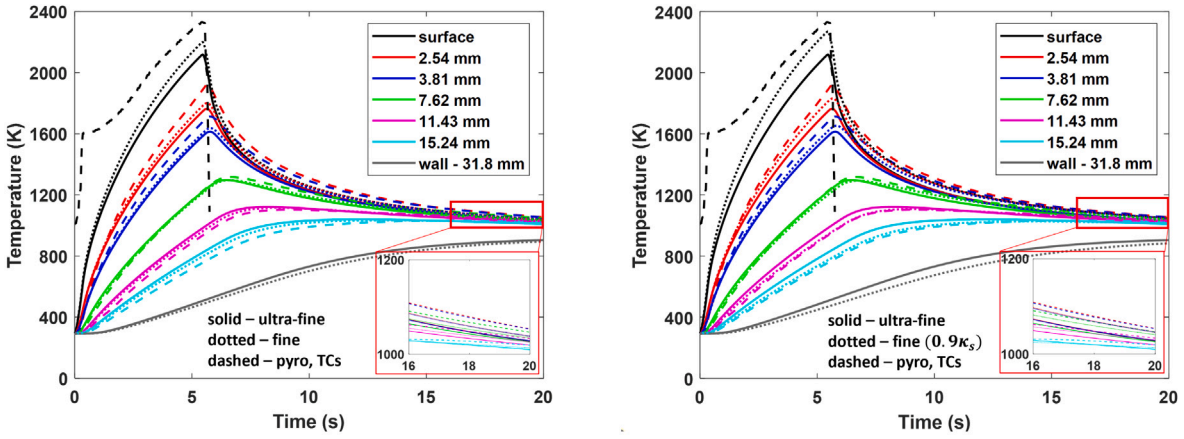

(a) Effect of fine-grade graphite conductivity.

(b) Effect of 10% reduction in conductivity of fine-grade graphite.

Fig. 18. Case 2 — effect of graphite conductivity on the temperature prediction with coupled approach (Le = 1).

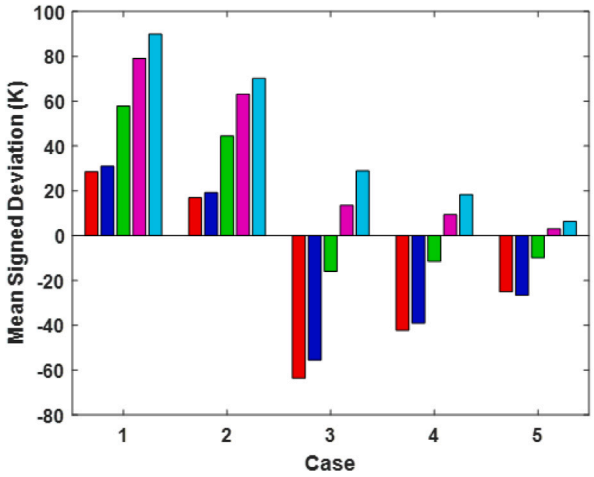

Fig. 19. Summary of uncertainty analysis presented as a Mean Signed Deviation of predicted temperatures from the thermocouples.

7. Conclusions

In this work, graphite ablation in an arc-jet flow was studied with coupled and uncoupled film-coefficient approaches using finite-rate and equilibrium surface ablation models. Two experimental test cases were explored consisting of a sphere-cone geometry exposed to a long-duration high enthalpy flow and an iso-q geometry, exposed for a much shorter duration to a lower heating environment. It was observed that the diffusion coefficient has a significant effect on the predicted material temperature and amount of surface ablation. In this work, a simplistic approach for the diffusion coefficient indicated that the unity Lewis number leads to a closer agreement with the experimental data and closer agreement between the two simulation approaches, especially at the stagnation region of the geometry. Away from the stagnation region, the uncoupled approach tends to deviate and predict lower temperatures and ablation rates which likely corresponds to the decreased performance of the film-coefficient approach and deviation from the equilibrium of the local chemical conditions.

Additionally, it was observed that the accuracy of the solution depends on the ablation regime of the material. In the sublimation regime, experienced at the nose section in the first case, the given models lead to a consistent overprediction of the surface temperatures and amount of recession. In the predominantly oxidation regime, experienced down the cone in the first case and the whole surface in the second case, the finite-rate simulations predict generally close agreement with the measured data. The role of the sublimation regime of the solution accuracy needs to be further investigated.

The scatter of thermo-physical properties of Poco graphite plays another significant role in the accuracy of the predictions. It was observed that a lower conductivity of the material (from the available sources) leads to a more accurate prediction of the measured data, assuming a unity Lewis number. Additionally, the available properties clearly do not cover the expected range of the material temperatures and the curve fits, used to extrapolate the data, incorporate additional sources of uncertainty.

In terms of the coupling scheme, the use of the surface chemistry module in the convergence of the near-body solver has improved the accuracy of the heating predictions and allowed the use of larger material time steps, without sacrificing the accuracy of the solution.

Finally, the diffusion-controlled regime observed in both problems implies that the diffusion coefficient plays a significant role not only in the predicted heating rate but also in the ablation rate of the material.

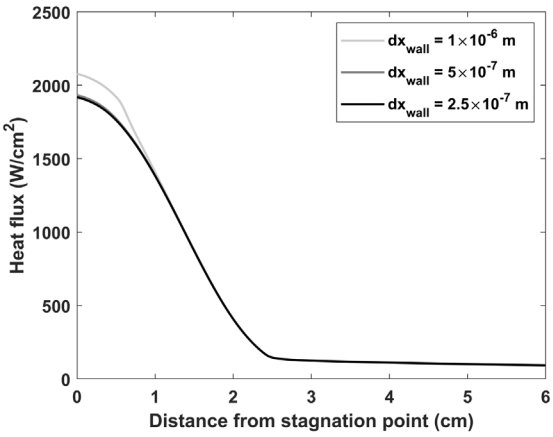

(a) Variable wall spacing (NBS = 100 points).

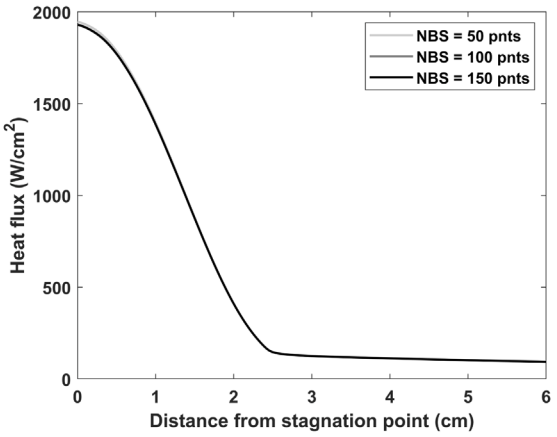

(b) Variable number of NBS points ($dx_{wall} = 5\times10^{-7}$ m).

Fig. 20. Case 1 — Heat flux prediction by NBS-Cart solver under varying levels of near-body grid resolution (T_{wall} = 312 K, Le = 1.4, non-catalytic wall).

In future studies, it can be interesting to explore the effect of higher fidelity transport properties on the coupled solution prediction.

Declaration of competing interest

The authors declare the following financial interests/personal relationships which may be considered as potential competing interests: Alexandre Martn reports financial support was provided by NASA Kentucky Space Grant and EPSCoR Programs. Christoph Brehm reports financial support was provided by NASA Kentucky Space Grant and EPSCoR Programs. Christoph Brehm reports financial support was provided by National Science Foundation.

Data availability

Data will be made available on request.

Acknowledgments

The authors would like to recognize and show appreciation for the financial support provided by NASA Kentucky EPSCoR RA, United States Award no. 80NSSC19M0144 (E. Stern technical monitor) and NASA EPSCoR R3 Award no. 80NSSC19M0084 (M. Barnhardt technical monitor). Christoph Brehm and Joel McQuaid would also like to recognize and show appreciation for the financial support provided by National Science Foundation, United States under award CBET-2146100 with Dr. R. Joslin as Program Manager. The authors would also like to thank Jonathan Morgan and Magnus Haw from the NASA Ames Research Center for providing measurement data and valuable discussions. Finally, the authors appreciate the University of Kentucky Center for Computational Sciences and Information Technology Services Research Computing for their support and use of the Lipscomb Compute Cluster and associated research computing resources.

Appendix A. Arrhenius curve fit coefficients

The forward reaction rate in Eq. (8) is computed using an Arrhenius curve fit for the Park two-temperature model as

$$k_{fr} = A_{fr} T_c^{\eta_r} \exp\left(-\frac{T_{ar}}{T_c}\right), \tag{30}$$

where,

$$T_c = T^{a_f} T_v^{b_f}. \tag{31}$$

Here, A_{fr} and η_r are coefficients for the Arrhenius curve fit, T_c is the forward controlling temperature, and T_{ar} represents the activation temperature. The values used for the Arrhenius curve fit can be found in Tables 6 and 7. The backward controlling reaction rate is a function of the forward reaction rate and the equilibrium constant, K_c, as computed using the backward controlling temperature, T_{bc},

$$k_{br}(T_{bc}) = \frac{k_{fr}(T_{bc})}{K_c(T_{bc})}, \tag{32}$$

where the backward controlling temperature is defined in Eq. (33) as

$$T_{bc} = T^{a_b} T_v^{b_b}. \tag{33}$$

For all dissociation reactions, the forward controlling temperature is computed using $a_f = 0.5$ and $b_f = 0.5$ whereas the backward dissociation reactions and all remaining exchange reactions are computed using $a_b = 1$ and $b_b = 0$. The equilibrium constant is computed using a NASA 9 polynomial curve fit for the normalized entropy and enthalpy of each species [68].

Table 7 shows the exchange reactions used in this work with their respective forward reaction rate coefficients. All exchange reactions are evaluated at the same controlling temperature defined by the translational/rotational temperature.

Appendix B. Thermal and transport properties

Tables 8 and 9 gives the coefficients for the curve fits in Eqs. (11) and (12) of thermal conductivity and surface emissivity of Poco graphite, based on the data in Sheppard et al. [47].

Table 10 gives the coefficients for carbon vaporization coefficient α_k in Eq. (19) and vaporization coefficients P_k and Q_k in Eq. (20) for each sublimation species.

Appendix C. Grid convergence study

Fig. 20 shows the results of the grid convergence study performed for the sphere-cone case. The convergence of the cold wall heat flux was achieved by varying the near-body grid resolution in terms of the wall spacing and the number of wall-normal nodes. Performance of the convergence study only in the near-body region was possible because the convergence of the off-body Cartesian grid is achieved automatically by using AMR and the requirement for the mesh refinement level to be high enough to comply with the NBS mesh size in the overset region. Based on the observed convergence, a wall spacing of 5×10^{-7} m and 100 points in the NBS layer were chosen to run all simulations.

Table 6
Arrhenius curve fit coefficients for dissociation reactions.

	Reaction	Partner	T_c	A_{fr} (cm^3/mol s)	η_r	T_{ar} (K)	Source
1	$N_2 + M \rightleftharpoons N + N + M$	molecules	$\sqrt{TT_v}$	7.00E21	−1.60	1.132E5	Ref. [69]
		atoms	$\sqrt{TT_v}$	3.00E22	−1.60	1.132E5	Ref. [69]
2	$O_2 + M \rightleftharpoons O + O + M$	molecules	$\sqrt{TT_v}$	2.00E21	−1.50	5.936E4	Ref. [69]
		atoms	$\sqrt{TT_v}$	1.00E22	−1.50	5.936E4	Ref. [69]
3	$NO + M \rightleftharpoons N + O + M$	other	$\sqrt{TT_v}$	5.00E15	0.00	7.550E4	Ref. [70]
		NO, CO_2, N, O, C	$\sqrt{TT_v}$	1.10E17	0.00	7.550E4	Ref. [70]
4	$C_3 + M \rightleftharpoons C_2 + C + M$	all	$\sqrt{TT_v}$	1.60E16	1.00	8.748E4	Ref. [71]
5	$CO_2 + M \rightleftharpoons CO + O + M$	molecules	$\sqrt{TT_v}$	1.40E22	−1.50	6.3280E4	Ref. [72]
		atoms	$\sqrt{TT_v}$	2.80E22	−1.50	6.3280E4	Ref. [72]
6	$C_2 + M \rightleftharpoons C + C + M$	all	$\sqrt{TT_v}$	3.70E14	0.00	6.9900E4	Ref. [73]
7	$CO + M \rightleftharpoons C + O + M$	all	$\sqrt{TT_v}$	3.00E21	−1.00	1.290E5	Ref. [72]
8	$CN + M \rightleftharpoons C + N + M$	all	$\sqrt{TT_v}$	2.50E14	0.00	7.100E4	Ref. [74]

Table 7
Arrhenius curve fit coefficients for exchange reactions.

	Reaction	T_c	A_{fr} (cm^3/mol s)	η_r	T_{ar} (K)	Source
9	$NO + O \rightleftharpoons O_2 + N$	T	2.49E9	1.18	4.010E3	Ref. [75]
10	$N_2 + O \rightleftharpoons NO + N$	T	6.00E13	0.10	3.8000E4	Ref. [76]
11	$CO + O \rightleftharpoons C + O_2$	T	3.90E13	−0.18	6.9200E4	Ref. [77]
12	$CN + O \rightleftharpoons NO + C$	T	1.60E12	0.10	1.4600E4	Ref. [72]
13	$CO_2 + O \rightleftharpoons O_2 + CO$	T	2.71E14	0.00	3.3800E4	Ref. [78]
14	$CO + C \rightleftharpoons C_2 + O$	T	2.00E17	−1.00	5.8000E4	Ref. [77]
15	$N_2 + C \rightleftharpoons CN + N$	T	1.10E14	−0.11	2.3200E4	Ref. [79]
16	$CN + C \rightleftharpoons C_2 + N$	T	5.00E13	0.00	1.3000E4	Ref. [74]
17	$CO + N \rightleftharpoons CN + O$	T	1.00E14	0.00	3.8600E4	Ref. [77]

Table 8
Curve fit coefficients for thermal conductivity of ultra-fine and fine-grade Poco graphite [47].

Coefficient	c_0	c_1	c_2
ultra-fine	45, 516.1	260.068	0.432289
fine	51 250.6	338.421	0.541335

Table 9
Curve fit coefficients for the surface emissivity of Poco graphite [47].

Coefficient	c_0	c_1
ultra-fine	0.794	2.28×10^{-5}

Table 10
Carbon vapor pressure coefficients [80].

	C	C_2	C_3
α_k	0.14	0.26	0.03
P_k	−85 715	−98 363	−93 227
Q_k	18.69	22.20	23.93

References

[1] Balter-Peterson A, Nichols F, Mifsud B, Love W. Arc jet testing in NASA Ames Research Center thermophysics facilities. In: AlAA 4th international aerospace planes conference. AIAA paper 1992-5041, 1992, http://dx.doi.org/10.2514/6.1992-5041.

[2] Park C, Raiche GA, Driver DM, Olejniczak J, Terrazas-Salinas I, Hightower TM, Sakai T. Comparison of enthalpy determination methods for an arc-jet facility. J Thermophys Heat Transfer 2006;20(4):672–9. http://dx.doi.org/10.2514/1.15744.

[3] Stewart D, Gokcen T, Chen Y-K. Characterization of hypersonic flows in the AHF and IHF of NASA ames arc-jet facilities. In: 41st AIAA thermophysics conference. AIAA paper 2009-4237, 2009, http://dx.doi.org/10.2514/6.2009-4237.

[4] Gokcen T, Chen Y-K, Skokova KA, Milos FS. Computational analysis of arc-jet stagnation tests including ablation and shape change. J Thermophys Heat Transfer 2010;24(4):694–707. http://dx.doi.org/10.2514/1.46199.

[5] Park C. Nonequilibrium hypersonic aerothermodynamics. 1989, http://dx.doi.org/10.1017/S0022112091230657.

[6] Park C. Assessment of a two-temperature kinetic model for dissociating and weakly ionizing nitrogen. J Thermophys Heat Transfer 1988;2(1):8–16. http://dx.doi.org/10.2514/3.55.

[7] Wright MJ, Candler GV, Bose D. Data-parallel line relaxation method for the Navier-Stokes equations. AIAA J 1998;36(9):1603–9. http://dx.doi.org/10.2514/2.586.

[8] Nompelis I, Drayna TW, Candler GV. A parallel unstructured implicit solver for hypersonic reacting flow simulation. In: Parallel computational fluid dynamics 2005. Elsevier; 2006, p. 389–95. http://dx.doi.org/10.2514/6.2005-4867.

[9] Scalabrin L, Boyd I. Numerical simulation of weakly ionized hypersonic flow for reentry configurations. In: 9th AIAA/ASME joint thermophysics and heat transfer conference. AIAA paper 2006-3773, 2006, http://dx.doi.org/10.2514/6.2006-3773.

[10] McQuaid JA, Zibitsker AL, Martin A, Brehm C. Heat flux predictions for high speed flows with an immersed boundary method. In: AIAA aviation forum. AIAA 2021-3145, AIAA; 2021, http://dx.doi.org/10.2514/6.2021-3145.

[11] Anderson L, Bartlett E, Kendall R, Nicolet W. Further studies of the coupled chemically reacting boundary layer and charring ablator. Part 1 - Summary final report. Technical Report NASA-CR-92471, NASA; 1968.

[12] Moyer CB, Rindal RA. An analysis of the coupled chemically reacting boundary layer and charring ablator. Part 2 - Finite difference solution for the in-depth response of charring materials considering surface chemical and energy balances. Contractor Report NASA-CR-1061, NASA; 1968.

[13] Bartlett E, Kendall R. An analysis of the coupled chemically reacting boundary layer and charring ablator. Part 3 - Nonsimilar solution of the multicomponent laminar boundary layer by an integral matrix method. Technical Report NASA-CR-1062, NASA; 1968.

[14] Kendall RM, Bartlett EP, Rindal RA, Moyer CB. An analysis of the coupled chemically reacting boundary layer and charring ablator, Part 1. Technical Report NAS 9-4599, Palo Alto, California: National Aeronautics and Space Administration; 1965.

[15] Blackwell B, Hogan R. One-dimensional ablation using Landau transformation and finite control volume procedure. J Thermophys Heat Transfer 1994;8(2):282–7. http://dx.doi.org/10.2514/3.535.

[16] Chen Y-K, Milos FS. Ablation and thermal response program for spacecraft heatshield analysis. J Spacecr Rockets 1999;36(3):475–83. http://dx.doi.org/10.2514/2.3469.

[17] Chen Y-K, Milos FS. Two-dimensional implicit thermal response and ablation program for charring materials. J Spacecr Rockets 2001;38(4):473–81. http://dx.doi.org/10.2514/2.3724.

[18] Amar A, Calvert N, Kirk B. Development and verification of the charring ablating thermal protection implicit system solver. In: 49th AIAA aerospace sciences meeting. AIAA 2011-144, 2011, http://dx.doi.org/10.2514/6.2011-144.

[19] Lachaud J, Mansour NN. Porous-material analysis toolbox based on OpenFOAM and applications. J Thermophys Heat Transfer 2014;28(2):191–202. http://dx.doi.org/10.2514/1.T4262.

[20] Weng H, Martin A. Multidimensional modeling of pyrolysis gas transport inside charring ablative materials. J Thermophys Heat Transfer 2014;28(4):583–97. http://dx.doi.org/10.2514/1.T4434.

[21] Schulz JC, Stern E, Muppidi S, Palmer G, Schroeder O, Martin A. Development of a three-dimensional, unstructured material response design tool. In: 55th AIAA aerospace sciences meeting. AIAA paper 2017-0667, 2017, http://dx.doi.org/10.2514/6.2017-0667.

[22] Ewing ME, Isaac DA, Heath Dewey H, Smith CW, Harman ZD, Walker DT. Multidimensional modeling of ablation heat transfer. J Thermophys Heat Transfer 2023;37(1):104–18. http://dx.doi.org/10.2514/1.T6582.

[23] Milos FS, Chen Y-K, Gokcen T. Nonequilibrium ablation of phenolic impregnated carbon ablator. J Spacecr Rockets 2012;49(5):894–904. http://dx.doi.org/10.2514/1.A32298.

[24] Zibitsker AL, McQuaid J, Brehm C, Martin A. Deviation from equilibrium thermochemistry and aerodynamic heating assumptions in the ablation process of camphor. In: AIAA aviation 2023 forum. AIAA paper 2023-3486, 2023, http://dx.doi.org/10.2514/6.2023-3486.

[25] Driver D, Olson M, Barnhardt M, MacLean M, MacLean M. Understanding high recession rates of carbon ablators seen in shear tests in an arc jet. In: 48th AIAA aerospace sciences meeting. AIAA paper 2010-1177, 2010, http://dx.doi.org/10.2514/6.2010-1177.

[26] Zibitsker AL, McQuaid JA, Brehm C, Martin A. Study of a two-dimensional shape change of blunt-body geometries at hypersonic conditions using fully-coupled simulation. In: AIAA aviation forum. AIAA paper 2022-4006, AIAA; 2022, http://dx.doi.org/10.2514/6.2022-4006.

[27] Chen Y-K, Milos FS, Gokcen T. Loosely coupled simulation for two-dimensional ablation and shape change. J Spacecr Rockets 2010;47(5):775–85. http://dx.doi.org/10.2514/1.39667.

[28] Chen Y-K, Milos FS. Navier-Stokes solutions with finite rate ablation for planetary mission earth reentries. J Spacecr Rockets 2005;42(6):961–70. http://dx.doi.org/10.2514/1.12248.

[29] Chen Y-K, Milos F, Reda D, Stewart D. Graphite ablation and thermal response simulation under arc-jet flow conditions. In: 36th AIAA thermophysics conference. AIAA paper 2003-4042, 2003, http://dx.doi.org/10.2514/6.2003-4042.

[30] Bianchi D, Nasuti F, Martelli E. Navier-Stokes simulations of hypersonic flows with coupled graphite ablation. J Spacecr Rockets 2010;47(4):554–62. http://dx.doi.org/10.2514/1.47995.

[31] Bersbach CJ, Evans J, Alkandry H, Ewing ME, Isaac DA. Ablative thermal response numerical modeling under arcjet test conditions. J Thermophys Heat Transfer 2022;1–10. http://dx.doi.org/10.2514/1.T6346.

[32] McQuaid JA, Zibitsker AL, Martin A, Brehm C. Simulation of graphite ablation using an overset near body solver on an adaptive block-structured cartesian off-body grid. In: AIAA aviation forum. AIAA; 2022, http://dx.doi.org/10.2514/6.2022-4088.

[33] Prata KS, Schwartzentruber TE, Minton TK. Air-carbon ablation model for hypersonic flight from molecular-beam data. AIAA J 2022;60(2):627–40. http://dx.doi.org/10.2514/1.J060516.

[34] Park C. Assessment of two-temperature kinetic model for ionizing air. J Thermophys Heat Transfer 1989;3:233–44. http://dx.doi.org/10.2514/3.28771.

[35] Hung C-M. Definition of contravarinat velocity components. In: 3rd theoretical fluid mechanics meeting. 2002, p. 3202. http://dx.doi.org/10.2514/6.2002-3202.

[36] Sutton K, Gnoffo PA. Multi-component diffusion with application to computational aerothermodynamics. In: 7th AIAA/ASME joint thermophysics and heat transfer conference. AIAA; 1998, http://dx.doi.org/10.2514/6.1998-2575.

[37] MacCormack RW, Candler GV. The solution of the Navier-Stokes equations using Gauss-Seidel line relaxation. Comput & Fluids 1989;17(1):135–50. http://dx.doi.org/10.1016/0045-7930(89)90012-1.

[38] Jiang G-S, Shu C-W. Efficient implementation of weighted ENO schemes. J Comput Phys 1996;126:202–28. http://dx.doi.org/10.1006/jcph.1996.0130.

[39] Ducros F, Ferrand V, Nicoud F, Weber C, Darracq D, Gacherieu C, Poinsot T. Large-eddy simulation of the shock/turbulence interaction. J Comput Phys 1999;152:517–49. http://dx.doi.org/10.1006/jcph.1999.6238.

[40] Zhang H, Reggio M, Trepanier J, Camarero R. Discrete form of the GCL for moving meshes and its implementation in CFD schemes. Comput & Fluids 1993;22(1):9–23. http://dx.doi.org/10.1016/0045-7930(93)90003-R.

[41] Cooper JM, Schroeder OM, Weng H, Martin A. Implementation and verification of a surface recession module in a finite volume ablation solver. In: 2018 joint thermophysics and heat transfer conference. 2018, p. 3272. http://dx.doi.org/10.2514/6.2018-3272.

[42] Zibitsker AL, McQuaid J, Brehm C, Martin A. Development and verification of a mesh deformation scheme for a three dimensional ablative material solver. In: AIAA SCITECH 2022 forum. AIAA paper 2022-1285, 2022, http://dx.doi.org/10.2514/6.2022-1285.

[43] Touloukian YS, Buyco EH. Specific heat - Nonmetallic solids. Technical Report ADA951939, Lafayette, IN: Thermophysical and electronic properties information analysis center; 1970.

[44] Touloukian YS, Powell RW, Ho CY, Klemens PG. Thermal conductivity - Nonmetallic solids. Technical Report ADA951936, Lafayette, IN: Thermophysical and electronic properties information analysis center; 1971.

[45] Touloukian YS, DeWitt DP. Thermal radiative properties - Nonmetallic solids. Technical Report ADA951942, Lafayette, IN: Thermophysical and electronic properties information analysis center; 1972.

[46] Taylor RE, Groot H. Thermophysical properties of POCO graphite. Technical Report ADA060419, Purdue University Lafayette Properties Research Lab; 1978, p. 21–2.

[47] Sheppard RG, Morgan D, Mathes DM, Bray DJ. Properties and characteristics of graphite for the EDM industry. Technical Report, POCO Graphite Inc.; 2002, URL: https://fliphtml5.com/ornh/ifkd/basic.

[48] Minyushkin DN, Kryukov IA. Calculation of aerodynamic heating and ablation of thermal protection system in axisymmetric formulation. In: AIP conference proceedings, Vol. 2181. AIP Publishing; 2019, http://dx.doi.org/10.1063/1.5135685.

[49] Murray VJ, Recio P, Caracciolo A, Miossec C, Balucani N, Casavecchia P, Minton TK. Oxidation and nitridation of vitreous carbon at high temperatures. Carbon 2020;167:388–402. http://dx.doi.org/10.1016/j.carbon.2020.05.076.

[50] Suzuki T, Fujita K, Ando K, Sakai T. Experimental study of graphite ablation in nitrogen flow. J Thermophys Heat Transfer 2008;22(3):382–9. http://dx.doi.org/10.2514/1.35082.

[51] Suzuki T, Fujita K, Sakai T. Experimental study of graphite ablation in nitrogen flow, part II: Further numerical analysis. J Thermophys Heat Transfer 2010;24(3):589–97. http://dx.doi.org/10.2514/1.43264.

[52] Baker RL. Graphite sublimation chemistry nonequilibrium effects. AIAA J 1977;15(10):1391–7. http://dx.doi.org/10.2514/3.60806.

[53] Anna A, Boyd I. Computation of surface catalysis for graphite exposed to high-enthalpy nitrogen flow. In: 50th AIAA aerospace sciences meeting. AIAA paper 2012-534, 2012, http://dx.doi.org/10.2514/6.2012-534.

[54] Sorensen C, Valentini P, Schwartzentruber TE. Uncertainty analysis of reaction rates in a finite-rate surface-catalysis model. J Thermophys Heat Transfer 2012;26(3):407–16. http://dx.doi.org/10.2514/1.T3823.

[55] Park C. Effects of atomic oxygen on graphite ablation. AIAA J 1976;14(11):1640–2. http://dx.doi.org/10.2514/3.7267.

[56] Park C. Calculation of stagnation-point heating rates associated with stardust vehicle. J Spacecr Rockets 2007;44(1):24–32. http://dx.doi.org/10.2514/1.15745.

[57] Zhluktov SV, Abe T. Viscous shock-layer simulation of airflow past ablating blunt body with carbon surface. J Thermophys Heat Transfer 1999;13(1):50–9. http://dx.doi.org/10.2514/2.6400.

[58] Schwartzentruber T. Nonequilibrium gas-surface interactions at high temperature. Technical Report AFRL-AFOSR-VA-TR-2020-0083, The University of Minnesota; 2020.

[59] Zibitsker AL, McQuaid J, Brehm C, Martin A. Fully-coupled simulation of low temperature ablator and hypersonic flow solver. In: AIAA SCITECH 2022 forum. AIAA paper 2022-0676, 2022, http://dx.doi.org/10.2514/6.2022-0676.

[60] Scoggins JB, Leroy V, Bellas-Chatzigeorgis G, Dias B, Magin TE. Mutation++: MUlticomponent Thermodynamic And Transport properties for IONized gases in C++. SoftwareX 2020;12. http://dx.doi.org/10.1016/j.softx.2020.100575.

[61] Kays WM, Crawford ME, Weigand B. Convective heat and mass transfer, Vol. 4. New York: McGraw-Hill; 1980.

[62] Cooper J, Salazar G, Martin A. Numerical investigation of film coefficient approximation for chemically reacting boundary-layer flows. J Thermophys Heat Transfer 2023;1–12. http://dx.doi.org/10.2514/1.T6707.

[63] Chilton TH, Colburn AP. Mass transfer (absorption) coefficients prediction from data on heat transfer and fluid friction. Ind Eng Chem 1934;26(11):1183–7.

[64] Askins LP, Martin A, Libben B, Palmer G, Williams J. Semi-empirical 1D material response modeling using inverse methods. In: AIAA AVIATION 2022 forum. AIAA paper 2022-3730, 2022, http://dx.doi.org/10.2514/6.2022-3730.

[65] Prabhu D, Saunders D, Oishi T, Skokova K, Santos J, Fu J, Terrazas-Salinas I, Carballo J, Driver D. CFD analysis framework for arc-heated flowfields I: stagnation testing in arc-jets at NASA ARC. In: 41st AIAA thermophysics conference. 2009, p. 4080. http://dx.doi.org/10.2514/6.2009-4080.

[66] Williams S, Curry DM. Thermal protection materials: Thermophysical property data. Technical Report NASA-RP-1289, S-693, NAS 1.61:1289, NASA Johnson Space Center; 1992.

[67] Bertin JJ, Bouslog SA, Wang K-C, Campbell CH. Recent aerothermodynamic flight measurements during Shuttle Orbiter re-entry. J Spacecr Rockets 1996;33(4):457–62. http://dx.doi.org/10.2514/3.26785.

[68] Gordon S, McBride BJ. Computer program for calculation of complex chemical equilibrium compositions and applications, Part I: Analysis. Technical Report NASA-RP-1311, NASA Lewis Research Center; 1994.

[69] Park C, Jaffe RL, Partridge H. Chemical-kinetic parameters of hyperbolic earth entry. J Thermophys Heat Transfer 2001;15:76–90. http://dx.doi.org/10.2514/2.6582.

[70] Park C, Howe JT, Jaffe RL. Chemical-kinetic problems of future NASA missions. In: 29th aerospace sciences meeting. AIAA paper 1991-464, 1991, http://dx.doi.org/10.2514/6.1991-464.

[71] Mitcheltree RA, Gnoffo PA. Wake flow about a MESUR mars entry vehicle. In: 6th AIAA/ASME joint thermophysics and heat transfer conference. AIAA; 1994, http://dx.doi.org/10.2514/6.1994-1958.

[72] Johnston CO, Brandis AM, Sutton K. Shock layer radiation modeling and uncertainty for mars entry. In: 43rd AIAA thermophysics conference. AIAA paper 2012-2866, AIAA; 2012, http://dx.doi.org/10.2514/6.2012-2866.

[73] Beck WH, Mackie JC. Formation and dissociation of C_2 from high temperature pyrolysis of acetylene. J Chem Soc Faraday Trans I 1975;71. http://dx.doi.org/10.1039/F19757101363.

[74] Mozzhukhin E, Burmeister M, Roth P. High temperature dissociation of cyanogen radical. Ber Bunsenges Phys Chem 1989;93:70–5.

[75] Bose D, Candler GV. Thermal rate constants of the $O_2 + N \rightarrow NO + O$ reaction based on the A2' and A4' potential-energy surfaces. J Chem Phys 1997;107:6136–45. http://dx.doi.org/10.1063/1.475132.

[76] Fujita K, Yamada T, Ishii N. Impacts of ablation gas kinetics on hyperbolic earth entry radiative heating. In: 44th AIAA aerospace sciences meeting and exhibit. AIAA paper 2006-1185, AIAA; 2006, http://dx.doi.org/10.2514/6.2006-1185.

[77] Park C, Howe JT, Jaffe RL. Review of chemical-kinetic problems of future NASA missions, II: Mars entries. J Thermophys Heat Transfer 1994;8:9–23. http://dx.doi.org/10.2514/3.496.

[78] Ibragimova LB. Recommended rate constants of $CO + O_2$ - reversible - $CO_2 + O$ reactions. Khim Fiz 1991;10:307–10.

[79] Park CS. Studies of radiation emission from the simulated shock layer of the huygens probe (Ph.D. thesis), Stanford, CA: Stanford University; 1991.

[80] Keenan J, Candler G. Simulation of graphite sublimation and oxidation under re-entry conditions. In: 6th joint thermophysics and heat transfer conference. AIAA paper 1994-2083, 1994, http://dx.doi.org/10.2514/6.1994-2083.